Investigation of the Effects of Slotted Solid Propellant's Sectional Geometry on Structural Strength and Internal Ballistic Performance of a Rocket Motor

Conference Paper · October 2016

CITATION
1

READS
1,041

2 authors:

Ceyhun Tola
ASELSAN Inc.
37 PUBLICATIONS **70** CITATIONS
SEE PROFILE

Melike Nikbay
Istanbul Technical University
123 PUBLICATIONS **837** CITATIONS
SEE PROFILE

INVESTIGATION OF THE EFFECTS OF SLOTTED SOLID PROPELLANT'S SECTIONAL GEOMETRY ON STRUCTURAL STRENGTH AND INTERNAL BALLISTIC PERFORMANCE OF A ROCKET MOTOR

CEYHUN TOLA

Department of Aeronautical and Astronautical Engineering, Istanbul Technical University
Istanbul, Turkey
tola@itu.edu.tr

MELİKE NİKBAY

Department of Astronautical Engineering, Istanbul Technical University
Istanbul, Turkey
nikbay@itu.edu.tr

Abstract

Relationship between the sectional geometric parameters of HTPB (Hydroxyl-terminated polybutadiene) based slotted solid rocket propellant on structural integrity and internal ballistic performance of a motor is examined benefiting from response surface method within the content of this study. Zero dimensional ballistic solver is developed and used to determine the effects of sectional geometric parameters on internal ballistic performance of the system. On the other hand, effects of the same parameters on structural strength of the system is also examined performing linear viscoelastic finite element analysis on *Abaqus* FEA (Finite Element Analysis) software environment under the assumption of plane strain. During finite element analysis, results of the zero dimensional internal ballistic analysis are used. Finally, different response surfaces are constructed to present graphical representations about the effects of sectional geometric parameters on solid propellant's structural strength and internal ballistic performance.

Keywords Solid Rocket Motor; Structural Strength; Viscoelasticity, Internal Ballistic Performance; 0-D Ballistic Solver; Response Surface.

1. Introduction

Solid rocket motors had become an indispensable part of propulsion systems since 1960s due to their reliability, low cost, ease of storage and fabrication. Currently, these motors are used on different systems such as: satellite launching systems, tactical missiles and ballistic rockets used for military purposes. Therefore, development of efficient solid rocket motors having lower mass and extended range has become an important issue. Development of an optimum solid rocket motor can be accomplished by first examining the effects of geometric parameters on structural strength and internal ballistic performance separately.

Within the content of this research, effects of a slotted sectional geometry, produced from HTPB (Hydroxyl-terminated polybutadiene) based solid propellant, on structural integrity and internal ballistic performance of a motor is examined. Structural integrity of the propellant is scrutinized performing linear viscoelastic analysis using finite element method via *Abaqus* FEA (Finite Element Analysis) software. On the other hand, internal ballistic performance analyzes are also performed using a 0-D internal ballistic solver which is developed on *Matlab* environment within the content of this work. As a result, different response surfaces are produced to summarize the effects of slotted solid propellant's sectional geometry on structural strength and internal ballistic performance of the rocket motor.

2. Structure of Solid Rocket Motors

A simple solid rocket motor mainly consists of five parts which are: motor case, insulation, igniter, nozzle and solid propellant. These parts can be seen from Fig. 1.

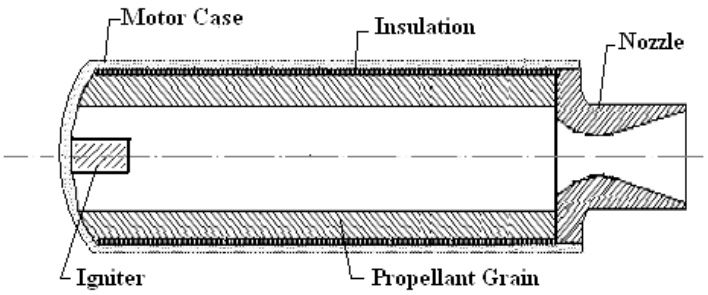

Fig. 1. Structure of a simple solid rocket motor (Acik, 2010).

Motor case covers insulation, igniter and solid propellant. Additionally, it endures high pressure and temperature loads governing from combustion process. Insulation isolates inner surface of the motor case from high temperature. Solid propellant stores chemical energy required to produce sufficient amount of thrust during the mission. Ignition process is performed by the igniter and thrust is provided by the nozzle by accelerating the combustion gasses through it.

3. Sectional Properties of Solid Propellants

Thrust profiles and structural strength of a solid rocket motor strongly depend on sectional geometry of the solid propellant. Various propellant geometries can be used on motors depending on the mission type. The sectional geometry of the solid propellant determines the variation of burn area; so, variation of chamber pressure and thrust profile also depend on the sectional geometry. Fig. 2. summarizes the alteration of thrust with respect to sectional properties of solid propellants.

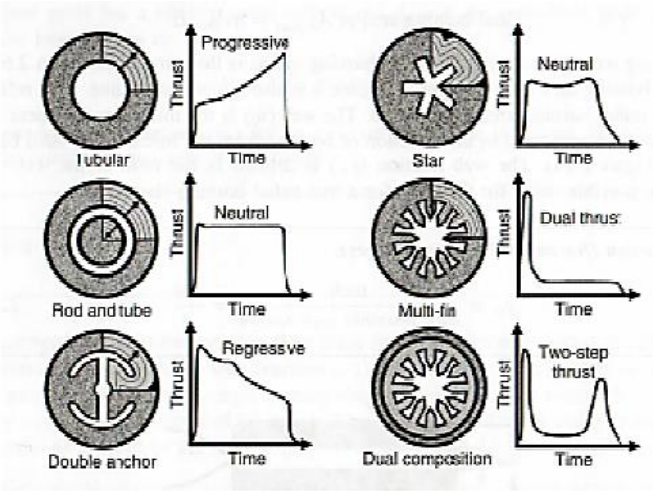

Fig. 2. Variation of thrust with respect to sectional properties of solid propellants (Ward, 2010).

Since variation of sectional geometry alters the chamber pressure, it also affects the structural strength of the propellant. Additionally, besides the change of chamber pressure owing from the geometry; structural strength of the solid propellant also depends on sectional geometry independent from the pressure load. For example, when the same chamber pressure is applied to different propellant geometries, different strain and stress results are determined owing to the geometry itself.

Within the content of this research, effects of sectional parameters on slotted grain shown in Fig. 3 are examined in terms of structural strength and internal ballistic performance using response surface method.

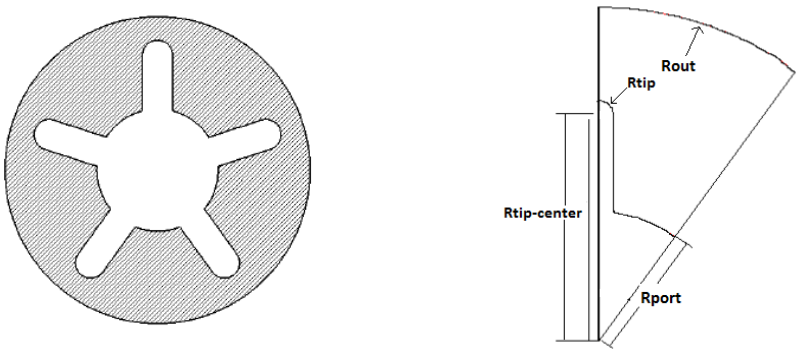

Cross Section Sectional Parameters

Fig. 3. Geometry of a slotted grain having 5 slots.

Slotted grain geometry consists of 1 discrete and 5 continuous sectional parameters. These are shown in Table I.

Table I. Sectional parameters of slotted grain.

Type	Parameter	Statement	Unit
Discrete	N	Number of slots	-
Continuous	L	Length of the propellant	mm
Continuous	R_{port}	Port radius (Inner radius)	mm
Continuous	R_{out}	Outer radius	mm
Continuous	R_{tip}	Tip radius of slot	mm
Continuous	$R_{tip\text{-}center}$	Slot length	mm

4. Mechanical Behavior of Solid Propellants

Investigation of the mechanical response of HTPB based solid rocket propellants under certain loading conditions can be accomplished using viscoelastic material models (AGARD-AR-350, 1997). Creep, stress relaxation, and relationship between strain and stress with time are expressed as main distinctive properties of viscoelastic materials (Lakes, 1999). Creep behavior can be described as the increment of strain under constant load while stress relaxation can be expressed as the decrement of stress under elongation load. These two significant phenomenon can be seen from Fig. 4.

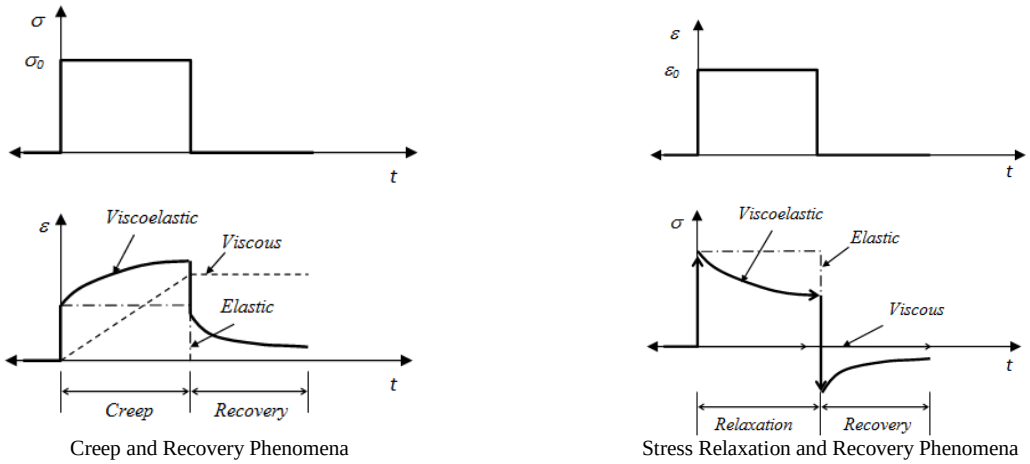

Creep and Recovery Phenomena Stress Relaxation and Recovery Phenomena

Fig. 4. Creep and stress relaxation phenomena (Ozgen, 2010).

5. Mechanical Characterization of Solid Propellants

Thermomechanical behavior of linear viscoelastic materials can be determined performing stress relaxation tests, uniaxial tension tests, thermomechanical analysis and different scanning calorimetry tests.

STANAG 4506 and 4507 NATO standards can be used to perform uniaxial tension tests and stress relaxation tests sequentially. Uniaxial tension tests are performed at different temperatures with different cross head speeds. On the other hand, stress relaxation tests are only performed at different temperatures. During the stress relaxation tests, specimen is extended up to 5% of its initial length and cross heads are fixed at that strain value by arranging magnitude of force on the cross heads. Relaxation behavior of the viscoelastic material at a certain temperature can be determined by reading the decrement of force values on the cross heads. Meanwhile, structural strength of the viscoelastic material can be determined performing uniaxial tension tests where test specimen is extended with constant cross head speed at a certain temperature until the specimen breaks up.

Results of the stress relaxation and uniaxial tension tests are used to construct the master curve of the propellant. The master curve contains mechanical properties of viscoelastic materials depending on temperature and time. A new variable called reduced time is defined in order to embed the temperature into the time domain. Superposition of stress relaxation and uniaxial tension tests performed at different temperatures can be accomplished via shift functions such as: Williams Landel Ferry (WLF) shift function given in Equation (1) (AGARD-AR-350, 1997).

$$\log(a_T) = \frac{-C_1(T - T_0)}{C_2 + (T - T_0)} \tag{1}$$

Where C_1 and C_2 are defined as empirical constants and T_0 represents the reference temperature. In this work, T_0 is taken as room temperature.

A simple mathematical expression called Prony Series written in Equation (2) can be constructed to represent the superposed stress relaxation test data (AGARD-AR-350, 1997).

$$E(t) = E_\infty + \sum_{i=1}^{N} E_i \cdot \exp\left(\frac{-t}{\lambda_i}\right) \tag{2}$$

E_i and λ_i's are relaxation modulus and time constants respectively. E_∞ is long term relaxation modulus value. Graphical representation of Prony Series can be shown in Fig. 5.

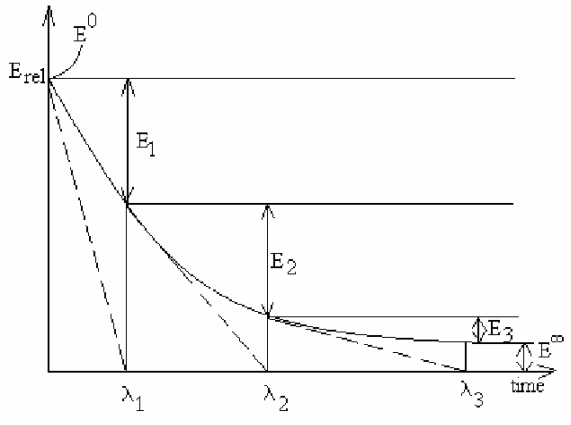

Fig. 5. Graphical representation of Prony Series (AGARD-AR-350, 1997).

Prony Series shown in Fig. 6 is used in finite element analysis to represent the relaxation behavior of the propellant.

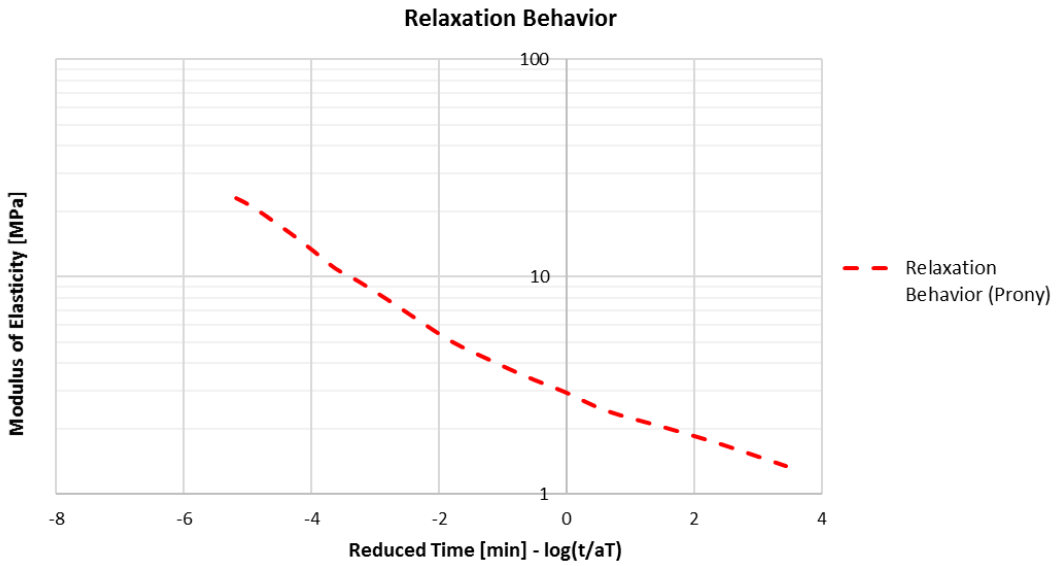

Fig. 6. Relaxation behavior of the propellant (Sutton and Biblarz, 2001).

Relaxation behavior shown in Fig. 6 is constructed normalizing the data on (Sutton and Biblarz, 2001).
Since the only aim of the study is to examine the effects of sectional parameters on slotted grain in terms of structural strength and internal ballistic performance; there are not any further evaluation methods needed to use to calculate the margin of safety values for structural analysis results. Therefore, uniaxial tension test data are not required for this study and so, they are not presented in Fig. 6.

Coefficient of thermal expansion of the propellant can be determined performing Thermomechanical Analysis (TMA) in accordance with ASTM standard, named ASTM E 831 and specific heat capacity of the propellant can be determined via Different Scanning Calorimetry (DSC) tests in accordance with ASTM E 1269 standard.

6. Internal Ballistics Performance Analysis

One of the practical methods to perform internal ballistic performance analysis of a solid rocket motor geometry is usage of a zero dimensional (0D) internal ballistic solver. Construction and usage of this kind of solver provides thrust profile, total impulse and specific impulse of the solid rocket motor.
In this study, zero dimensional internal ballistic solver is developed to perform the performance analysis of slotted grains having different sectional parameters. Following assumptions are made during the development of the solver:

- Combustion gasses are assumed as ideal gasses.
- Properties of the combustion gasses are not varying through the motor.
- Effects of erosive burning is neglected.
- Inertia of the combustion gasses are neglected.
- Flow through the nozzle is assumed as steady, one dimensional and isentropic.
- Relation between the chamber pressure and burning rate (r_b) can be explained according to the Saint Robert's burn rate law. Equation (5) represents the Saint Robert's burn rate law (Sutton and Biblarz, 2001):

$$r_b = a \cdot P_C{}^n \tag{5}$$

Where, P_C refers chamber pressure and a and n are empirical coefficients varying according to type of the propellant.
Using conservation of mass, combustion process of the solid rocket motor can be illustrated as in Fig. 7 and examining this figure, Equation (6) can be written as follows:

$$\dot{m}_g = \frac{dM}{dt} + \dot{m}_n \tag{6}$$

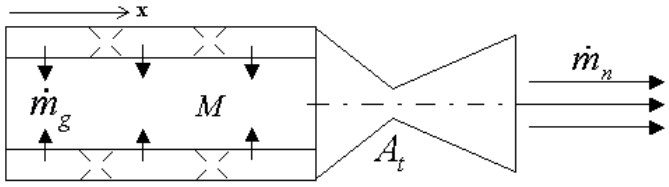

Fig. 7. Conservation of mass (Toker, 2004).

Where, $\dot{m}_g$ represents the mass flow rate of the propellant, *dM/dt* stands for the variation of mass of the stored propellant with respect to time, and $\dot{m}_n$ represents the mass flow through the nozzle. All of the terms in Equation (6) can be written as in Equations (7), (8) and (9).

$$\dot{m}_g = \rho_p \cdot A_b \cdot r_b = \rho_p \cdot A_b \cdot a \cdot P_c^{\,n} \tag{7}$$

$$\dot{m}_n = \frac{P_c \cdot A_t}{c^*} \tag{8}$$

$$\frac{dM}{dt} = \frac{d(\rho_g V_p)}{dt} = \rho_g \frac{d(V_p)}{dt} + V_p \frac{d(\rho_g)}{dt} \tag{9}$$

Additionally, making an ideal gas assumption, Equation (10) can also be written.

$$\rho_g = \frac{P_c}{R \cdot T_c} \tag{10}$$

Combining Equations (7) to (10) in Equation (6), Equation (11) can be determined (Sutton and Biblarz, 2001).

$$\frac{dP_c}{dt} = \frac{1}{V_i}\left[R \cdot T_c \cdot \left(\rho_p \cdot A_b \cdot a \cdot P_c^{\,n} - \frac{P_c \cdot A_t}{c^*} \right) - P_c \frac{dV_i}{dt} \right] \tag{11}$$

Where, chamber pressure and chamber temperature are denoted as P_c and T_c respectively. ρ_p represents density of the solid propellant and A_b and A_t refer burning area and nozzle throat area respectively. R denotes gas constant and V_i refers gas volume (port volume). a and n are empirical constants governing from the Saint Robert's burn rate law.

In order to solve the Equation (11), variation of burning area and gas volume with respect to time is required. This information is provided from burnback analysis solutions that are accomplished using analytical formulas.

After the variation of chamber pressure with respect to time is calculated, nozzle exit pressure (P_e) will be calculated using nozzle dimensions, as in Equation (12) (Sutton and Biblarz, 2001):

$$\frac{A_t}{A_e} = \left(\frac{\gamma+1}{2} \right)^{\frac{1}{\gamma-1}} \cdot \left(\frac{P_e}{P_c} \right)^{\frac{1}{\gamma}} \cdot \sqrt{ \frac{\gamma+1}{\gamma-1} \cdot \left[1 - \left(\frac{P_e}{P_c} \right)^{\frac{\gamma-1}{\gamma}} \right] } \tag{12}$$

Then, thrust coefficient (C_F) is calculated using Equation (13) (Sutton and Biblarz, 2001):

$$C_F = \sqrt{ \frac{2\gamma^2}{\gamma-1} \cdot \left[\frac{2}{\gamma+1} \right]^{\frac{\gamma+1}{\gamma-1}} \cdot \left\{ 1 - \left[\frac{P_e}{P_c} \right]^{\frac{\gamma-1}{\gamma}} \right\} } + \frac{P_e - P_{amb}}{P_c} \cdot \varepsilon \tag{13}$$

Where, γ defined as ratio of specific heats, P_e denotes nozzle exit pressure, P_{amb} represents ambient pressure and ε refers the ratio of A_e/A_t.

After that, variation of thrust is calculated using Equation (14) (Sutton and Biblarz, 2001):

$$F = C_F \cdot P_c \cdot A_t \tag{14}$$

Where A_t denotes throat area of the nozzle.
Finally, total impulse (I_t) and specific impulse (I_{sp}) values of the solid rocket motor are evaluated using Equation (15) and (16) respectively (Sutton and Biblarz, 2001):

$$I_t = \int_0^t F \cdot dt \tag{15}$$

$$I_{sp} = \frac{c^* \cdot C_F}{g_0} \tag{16}$$

Where c^* denotes characteristic velocity and g_0 refers gravitational acceleration.
Production of high specific impulse with lower solid propellant mass is an indication of high efficiency.

6.1. *Grain Burnback Analysis*

Variation of burn area (A_b) and port volume (V_i) with respect to time have to be calculated accurately in order to integrate Equation (11) and to calculate the thrust profile accurately. This is possible by performing burnback analysis.
After the ignition of the solid rocket motor, burning area regresses perpendicular to itself and so, volume of the solid propellant decreases while port volume (gas volume) increases with respect to time. The only way to numerically examine this process is to perform burnback analysis.
Although different burnback methods such as: analytical, numerical and drafting techniques can be used to examine the variation of burn area (A_b) and port volume (V_i) with respect to time; analytical methods are preferred within the content of this research since they provide exact solutions in a short time for simple geometries without requiring any CAD or mesh software usage. By the way, usage of analytical method requires development of different analytical formulas for various grain burnback probabilities. Within the content of this research, it is determined that there are 12 different possible burnback scenarios for slotted grains having different geometric parameters. Each of the scenarios has 3 or 4 phases and usually, the last two phases are belong to the solution of the sliver region while the first phase is common for them. Fig. 8 represents three of these different scenarios as sample.

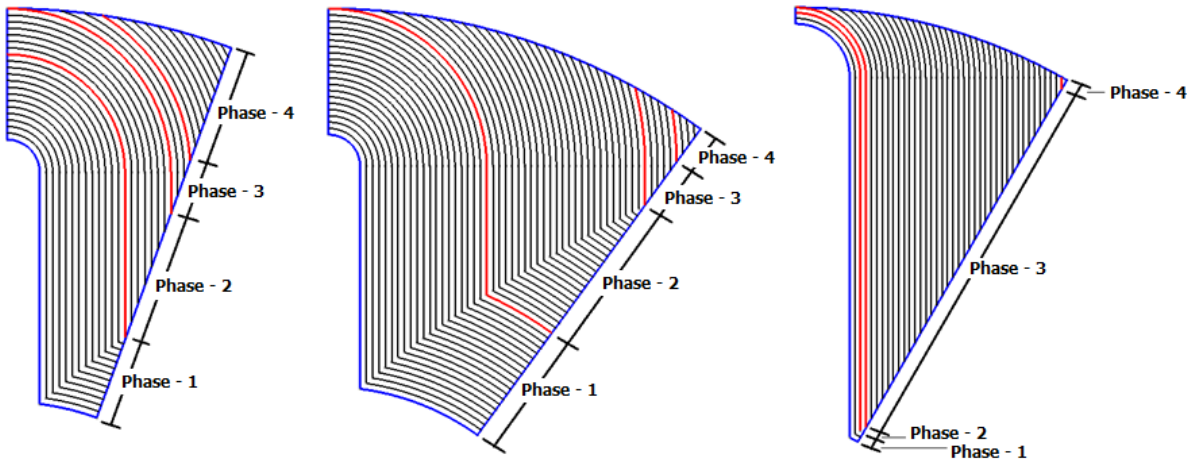

Fig. 8. Sample burnback scenarios for different sectional geometries.

Since the aim of this research is to examine the effects of sectional parameters on slotted grain in terms of structural strength and internal ballistic performance using response surface method; derivation and validation of burnback expressions is beyond the scope of this research and so, these are not presented in this work.

6.2. *Inputs of the 0D Internal Ballistic Solver and Results of Sample Run*

Parameters used in the zero dimensional internal ballistic solver is listed in Table II.

Table II. Input parameters used in 0D internal ballistic solver (Gandia, 2012).

Symbol	Parameter	Value	Unit
T_C	Chamber Temperature	3370	K
ρ_p	Density of the Propellant	1700	kg/m^3
R	Gas Constant	284	J/kg.K
γ	Ratio of Specific Heats	1.17	-
c^*	Characteristic Velocity	1575	m/s
n	Burning Rate Exponent	0.4	-
$r_{b\text{-}ref}$	Reference Burning Rate @ 1000 PSI	15	mm/s
A_e/A_t (ε)	Ratio of Nozzle Exit Area to Nozzle Throat Area	4	-

In order to get an idea about the sample results of the solver, a slotted grain geometry whose parameters are listed in Table III is analyzed and results of it are represented in Figure 9.

Table III. Sectional parameters used for the sample internal ballistic analysis.

Symbol	Parameter	Value	Unit
R_{out}	Outer radius	100	mm
R_{port}	Inner (Port) radius	40	mm
$R_{tip\text{-}center}$	Distance between center of slot tip radius to center of the propellant (Slot length)	75	mm
R_{tip}	Slot tip radius	5	mm
N	Number of slots	5	-
L	Length	1000	mm

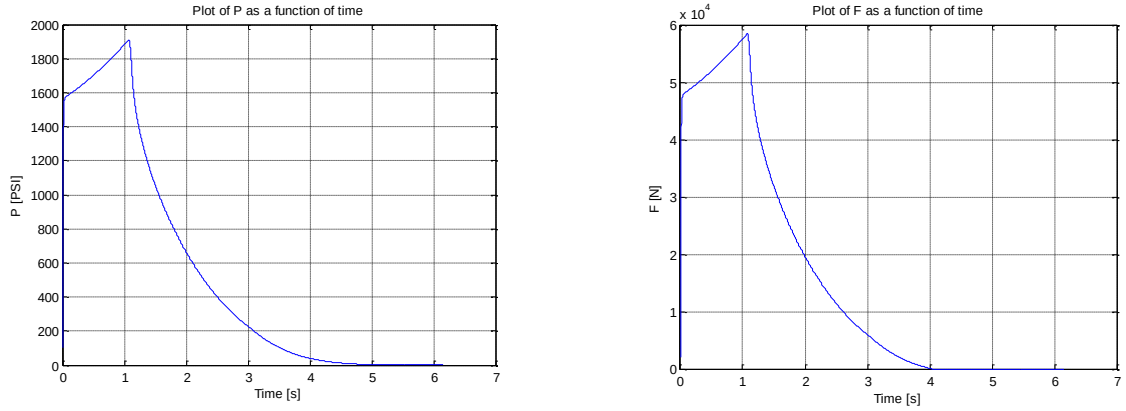

Variation of Chamber Pressure with Respect to Time — Variation of Thrust with Respect to Time

Fig. 9. Sample 0D internal ballistic analysis results.

Sudden pressure increment just after the ignition process can be seen from Fig. 9. Since the solid propellant has viscoelastic behavior, not only magnitude of the pressure load but also its application time (rise time of the pressure - t_{rise}) have significant effect on the structural strength of the design. Therefore, the first steepest peak point of the pressure value (P) and rise time corresponding to that pressure (t_{rise}) is used for the ignition step of finite element analysis.

7. Structural Strength Analysis

7.1. *Geometry and Modelling*

Structural strength analysis of slotted grains having a constant outer radius (R_{out}) and different number of slots (N), port radius (R_{port}), tip radius (R_{tip}) and slot center radius ($R_{tip\text{-}center}$) values are analyzed using finite element method in order to construct response surface. *Abaqus* FEA software is used as FEA solver and linear viscoelastic models are prepared in that environment.
Since the shape of the slotted geometry is suitable for modelling with symmetry boundary conditions and this process decreases solution time without making any concessions from accuracy of the solution; within the content of this research, grain geometries are prepared using symmetry boundary conditions. The logic of symmetric modeling can be shown in Fig. 10. Additionally, section of the grain is analyzed by making plane strain assumption which is suitable for this problem.

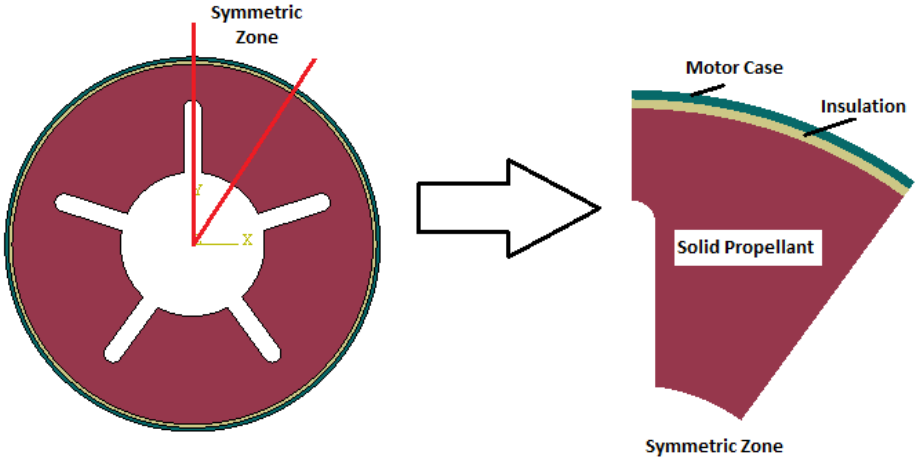

Fig. 10. Symmetric modelling.

7.2. *Loading Conditions*

Two different loading conditions are examined which are cooling and ignition processes.

7.2.1. *Cool-down process*

During the cooling process, the solid rocket motor is cooled down from the propellant's stress – strain free temperature (taken as *331 K*) to its minimum operating temperature (assumed as *233 K*). Thus, maximum strain and stress levels on the propellant during cool-down process are determined.
In order to perform viscoelastic solution of the cooling process and to determine stress and strain levels of this loading condition; cool-down time of the rocket motor and variation of the system's temperature with respect to time have to be determined performing heat transfer analysis before the viscoelastic solutions. Therefore, within the content of this research, different heat transfer models are also constructed corresponding to different sectional geometric parameter values and results of these models are used in the cool-down step of the viscoelastic models. Details of the heat transfer model are explained in the sub-heading of *"Heat transfer model"*.

Heat transfer model: During the real cool-down applications, special refrigeration cabinets blowing cold-air with constant speed are used for cooling rocket motors to desired temperature. In order to simulate the real process as accurate as possible, forced convection problem over a cylinder is prepared and solved. Quadratic heat transfer elements consisting 8 nodes (*DC2D8*) and having maximum dimensions of 2 mm are preferred to construct the heat transfer model.

Average forced convection coefficient needs to be calculated in order to determine the cool-down duration of the propellant's most inner nodes. Following process summarizes the calculation of average forced convention coefficient (Incropera and DeWitt, 2007).

$$T_{initial} = 331K \tag{17}$$

$$T_{final} = 233K \tag{18}$$

$$T_{film} = \frac{T_{initial} + T_{final}}{2} = 282K \tag{19}$$

Using the appendix tables in (Incropera and DeWitt, 2007) reference and performing interpolation for the film temperature (T_{film}), kinematic viscosity (v), thermal conduction coefficient (k) and Prandtl number (Pr) for air is calculated as in Table IV.

Table IV. Calculation of *v, k* and *Pr* parameters at film temperature (Incropera and DeWitt, 2007).

	T_1 = 250K	T_2 = 300K	T_{film} = 282K
Kinematic Viscosity [m²/s]	$v_1 = 11.44 \cdot 10^{-6}$	$v_2 = 15.89 \cdot 10^{-6}$	$v_{film} = 14.29 \cdot 10^{-6}$
Thermal Conduction Coefficient [W/m.K]	$k_1 = 22.3 \cdot 10^{-3}$	$k_2 = 26.3 \cdot 10^{-3}$	$k_{film} = 24.9 \cdot 10^{-3}$
Prandtl Number	$Pr_1 = 0.720$	$Pr_2 = 0.707$	$Pr_{film} = 0.712$

It is assumed that, the refrigeration cabinet is blowing air with a constant speed of 2 m/s and outer diameter of the rocket motor is fixed as 205 mm. Using these information, average forced convection coefficient is calculated as follows.

$$\mathrm{Re}_D = \frac{u_\infty \cdot D}{\nu_{film}} \cong 28695 \tag{20}$$

$$\overline{Nu}_D = 0.3 + \frac{0.62 \cdot \mathrm{Re}_D^{\frac{1}{2}} \cdot \mathrm{Pr}^{\frac{1}{3}}}{\left[1 + (0.4/\mathrm{Pr})^{\frac{2}{3}}\right]^{\frac{1}{4}}} \cdot \left[1 + \left(\frac{\mathrm{Re}_D}{282000}\right)^{\frac{5}{8}}\right]^{\frac{4}{5}} \cong 98.097 \tag{21}$$

$$\bar{h} = \frac{\overline{Nu}_D \cdot k}{D} \cong 11.896 W/m. \cdot K \tag{22}$$

The convection coefficient is applied to the outer surface of the motor case and results of the heat transfer analysis are showed that there is an exponential temperature decrement at the most inner nodes of the solid propellant as it is shown in Fig. 11. Fig. 11 and Fig. 12 represents the sample heat transfer analysis results belonging to the sectional geometry whose dimensions were listed in Table III previously.

Inner nodes of the propellant determine the cool down time of the system as it can be seen from Fig. 12.

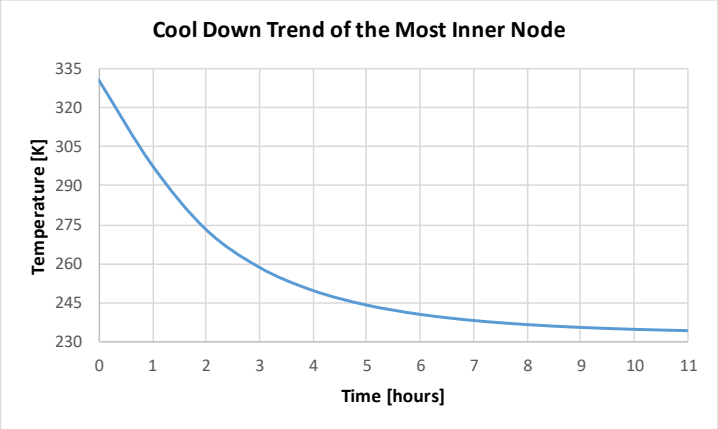

Fig. 11. Sample cool-down graph.

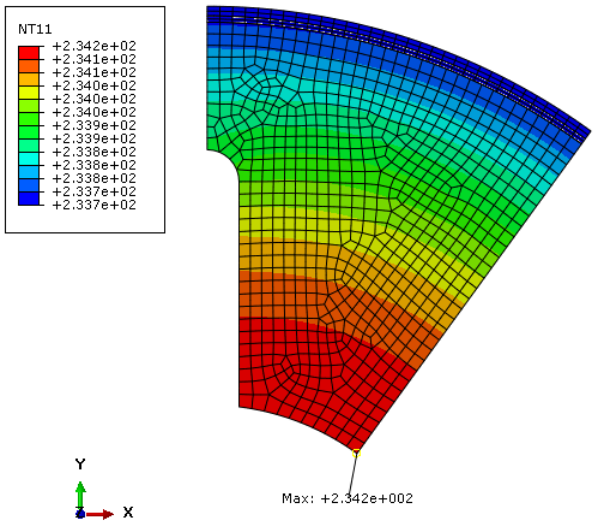

Fig. 12. Sample heat transfer analysis result [K].

7.2.2. *Ignition process*

After the cool-down step, the first steepest peak value of the chamber pressure (P) (shown in Fig. 8) coupled with the rise time of that pressure value (t_{rise}) is applied to burning area of the propellant and maximum strain and stress values are determined. Input values of this step is provided from the internal ballistic analysis results.

7.3. *Boundary Conditions and Mesh*

Linear viscoelastic analysis belonging to different grain configurations are performed using the results of heat transfer analysis for cool down step and the results of internal ballistic solver for ignition (pressurization) step. HTPB based solid propellant is modeled from 8 node quadratic plain strain elements having hybrid formulation and reduced integration (*CPE8RH*). Insulation and motor case are constructed from 8 node quadratic plane strain elements having full integration (*CPE8*). Same mesh dimensions are used for both heat transfer and viscoelastic finite element analysis models in order to prevent errors governing from interpolation of the heat transfer results on viscoelastic FEA model.

Locations of symmetry boundary conditions and pressure load with mesh structure belonging to one of the grain configuration whose dimensions were listed in Table III previously can be seen from Fig. 13.

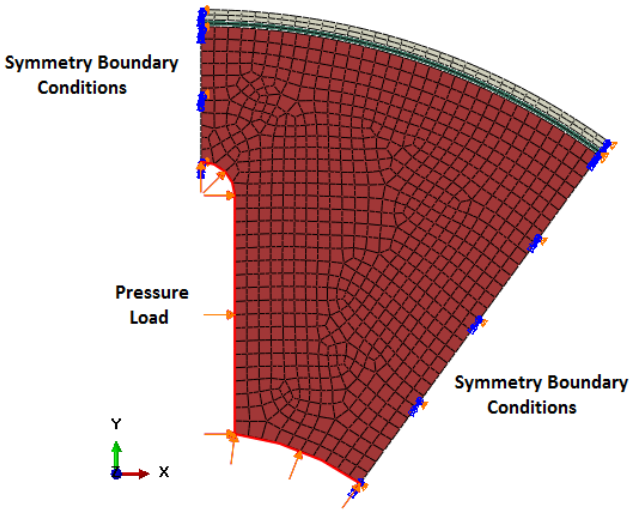

Fig. 13. Boundary conditions, pressure load and mesh structure of sample FEA model.

7.4. *Sample Finite Element Analysis Results*

In order to get an idea about the sample results belonging to the ignition step of the finite element analysis; the slotted grain geometry whose parameters were previously listed in Table III is analyzed and results of it are represented in Figure 14.

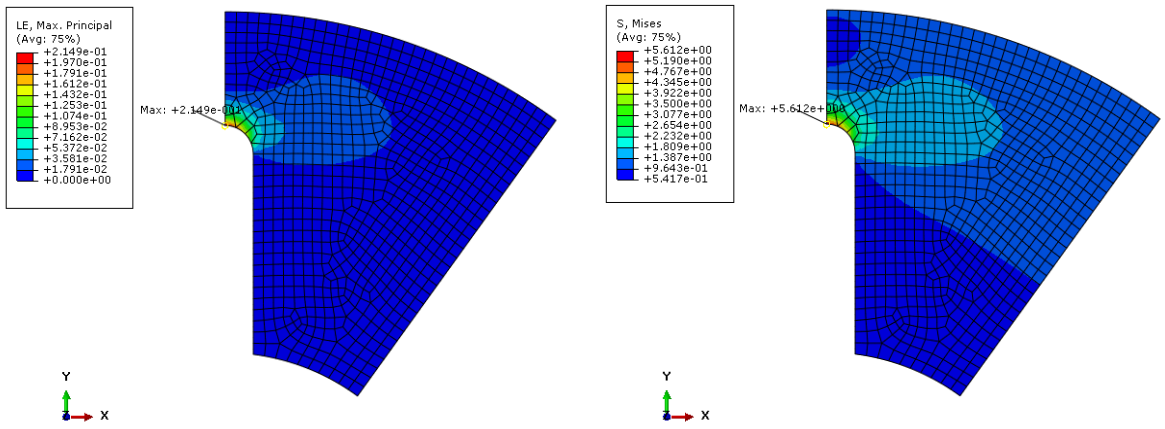

Max. Principal Strain Von Misses Stress [MPa]

Fig. 14. Sample viscoelastic analysis result belonging to ignition step.

Fig. 14 represents that the critical point in terms of both strain and stress is at the top of the slot radius.

8. Flow Scheme of the Process

In order to construct response surfaces of internal ballistic performance and structural strength analysis results, numerous sections having different dimensions have to be modeled and analyzed separately. Since manually accomplishment of this process takes a lot of time, *Process Modeler* software is used to automate the solution process. Fig. 15 represents the flow scheme of the automated process.

As it can be seen from Fig. 15 that automated process consists of 3 steps. Internal ballistic solution is performed using a *Matlab* code in the first step. Thus, mass of the propellant, specific impulse of the rocket motor (I_{sp}), pressure value at the first steepest peak point (P) and rise time corresponding to that pressure (t_{rise}) are calculated in this step. After that, heat transfer and viscoelastic finite element analysis are performed using *Abaqus* FEA software sequentially. *Pytheon* scripts are prepared and used within the content of this research in order to construct parametric finite element models for both heat transfer and viscoelastic analysis purposes.

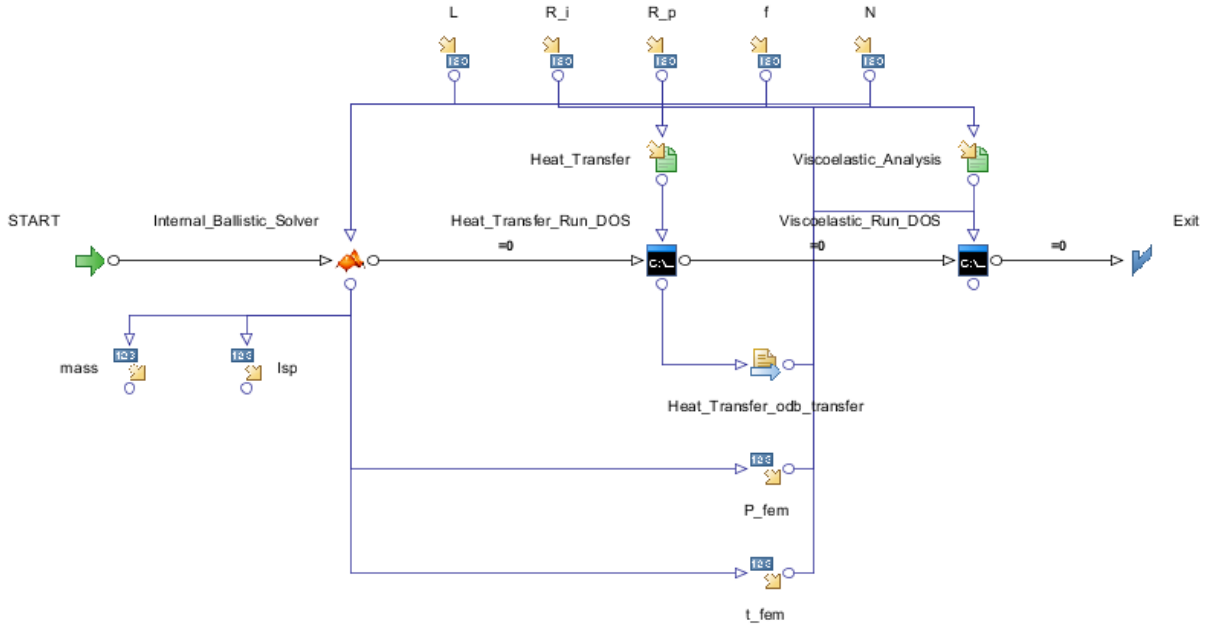

Fig. 15. Flow scheme of the automated solution process.

9. Response Surface Analysis

Response surface method is used to determine detailed information of the effects of explanatory variables on a response variable. Thus, usage of this method facilitates the work of designers.

Within the content of this work different response surfaces are prepared to examine the effects of sectional parameters on response variables.

Before examining the response surface results, it will be helpful to review Table V where parameters located in response surfaces and their units are summarized.

Table V. Response surface parameters and units.

Symbol	Parameter	Unit
R_{port}	Inner (Port) radius	mm
$R_{tip\text{-}center}$	Distance between center of slot tip radius to center of the propellant (Slot length)	mm
R_{tip}	Slot tip radius	mm
N	Number of slots	-
L	Length of the propellant	mm
I_{sp}	Specific impulse	s
P	Chamber pressure value at the first steepest peak point	MPa
t_{rise}	Rise time corresponding to P	s
Mass	Mass of the propellant	kg
Eff. Strain	Maximum effective strain	-
VM Stress	Von Misses stress	MPa

9.1. *Response Surfaces Belonging to Internal Ballistic Performance Results*

In this sub-section, 4 different response surface analysis are performed using internal ballistic performance analysis results.

9.1.1. *Response surface of specific impulse (I_{sp})*

Fig. 16 represents the percentage effects of sectional parameters and interactions of them on specific impulse results.

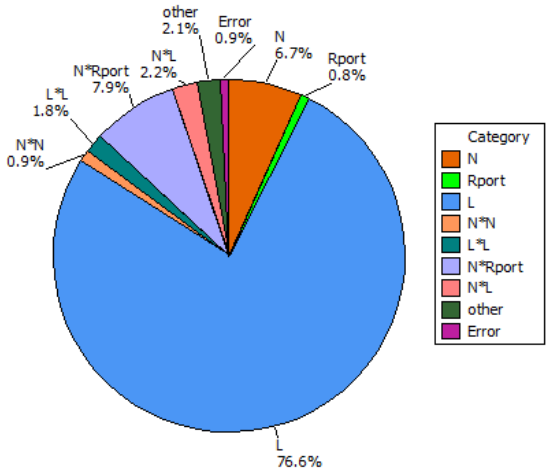

Fig. 16. Effects of sectional parameters and interactions of them on specific impulse (I_{sp}).

Fig. 17 represents the variation of specific impulse results with respect to sectional parameters.

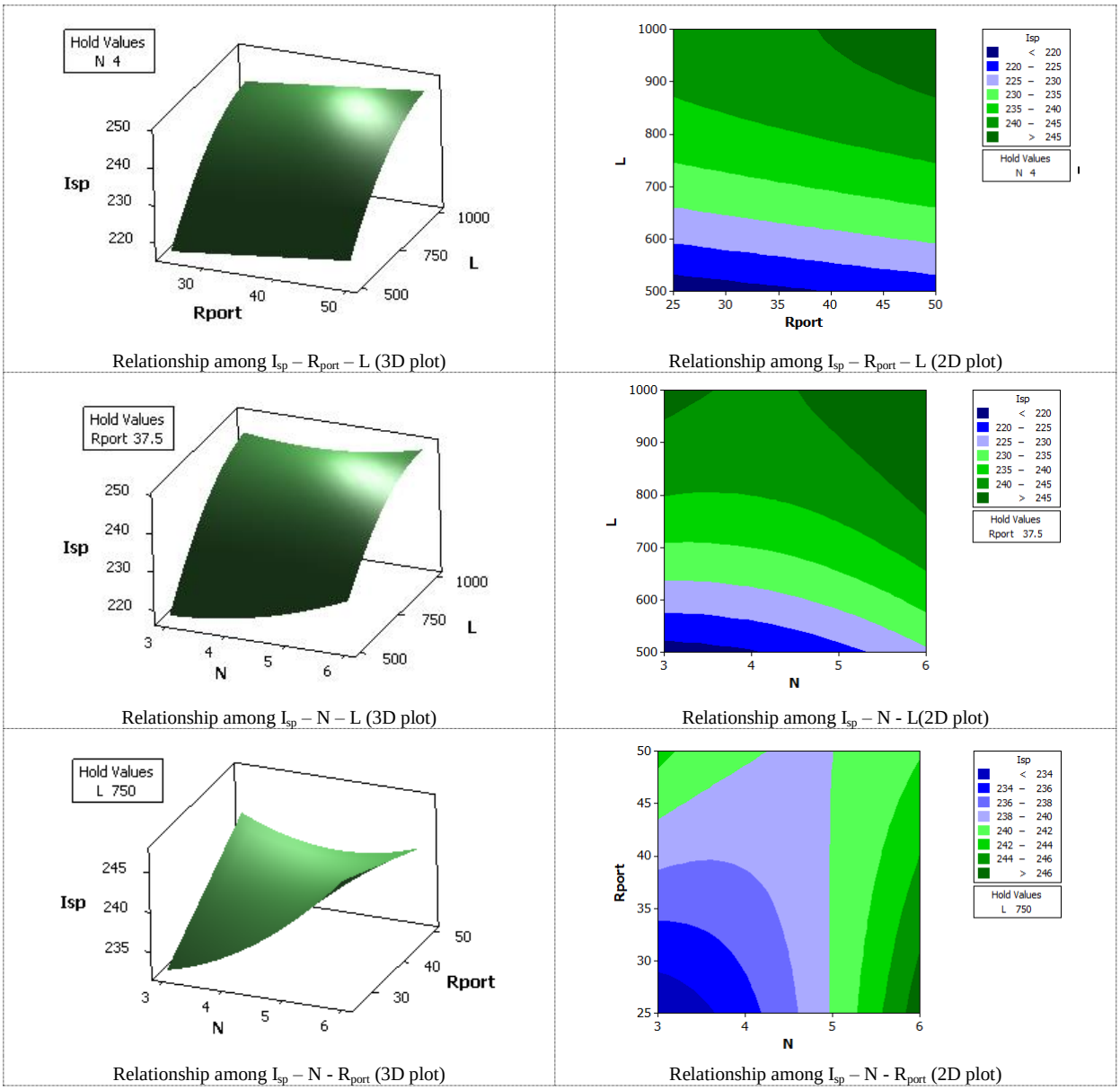

Relationship among I_{sp} – R_{port} – L (3D plot)

Relationship among I_{sp} – R_{port} – L (2D plot)

Relationship among I_{sp} – N – L (3D plot)

Relationship among I_{sp} – N - L(2D plot)

Relationship among I_{sp} – N - R_{port} (3D plot)

Relationship among I_{sp} – N - R_{port} (2D plot)

Fig. 17. Effects of parameters and interactions of them on specific impulse (I_{sp}).

Fig. 16 and Fig. 17 can be commented as follows:

- Length of the propellant (L) has the greatest effect on specific impulse (I_{sp}) variation.
- Increment of length (L), number of slots (N) and inner (port) radius (R_{port}) increases specific impulse.

9.1.2. *Response surface of chamber pressure value at the first steepest peak point (P)*

Chamber pressure value at the first steepest peak point (P) is one of the important parameters that should be examined since this parameter has a critical importance on structural strength results of the system.
Fig. 18 represents the percentage effects of sectional parameters and interactions of them on chamber pressure value at the first steepest peak point (P).

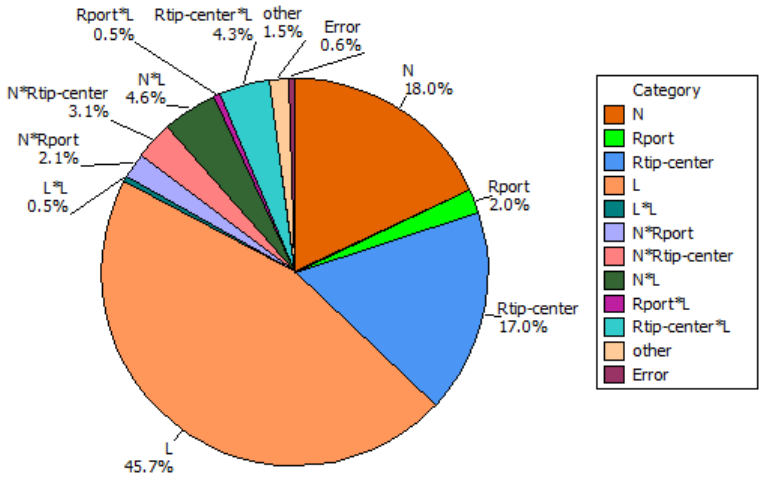

Fig. 18. Effects of sectional parameters and interactions of them on chamber pressure value at the first steepest peak point (P).

Fig. 19 represents the variation of chamber pressure value at the first steepest peak point (P) with respect to sectional parameters.

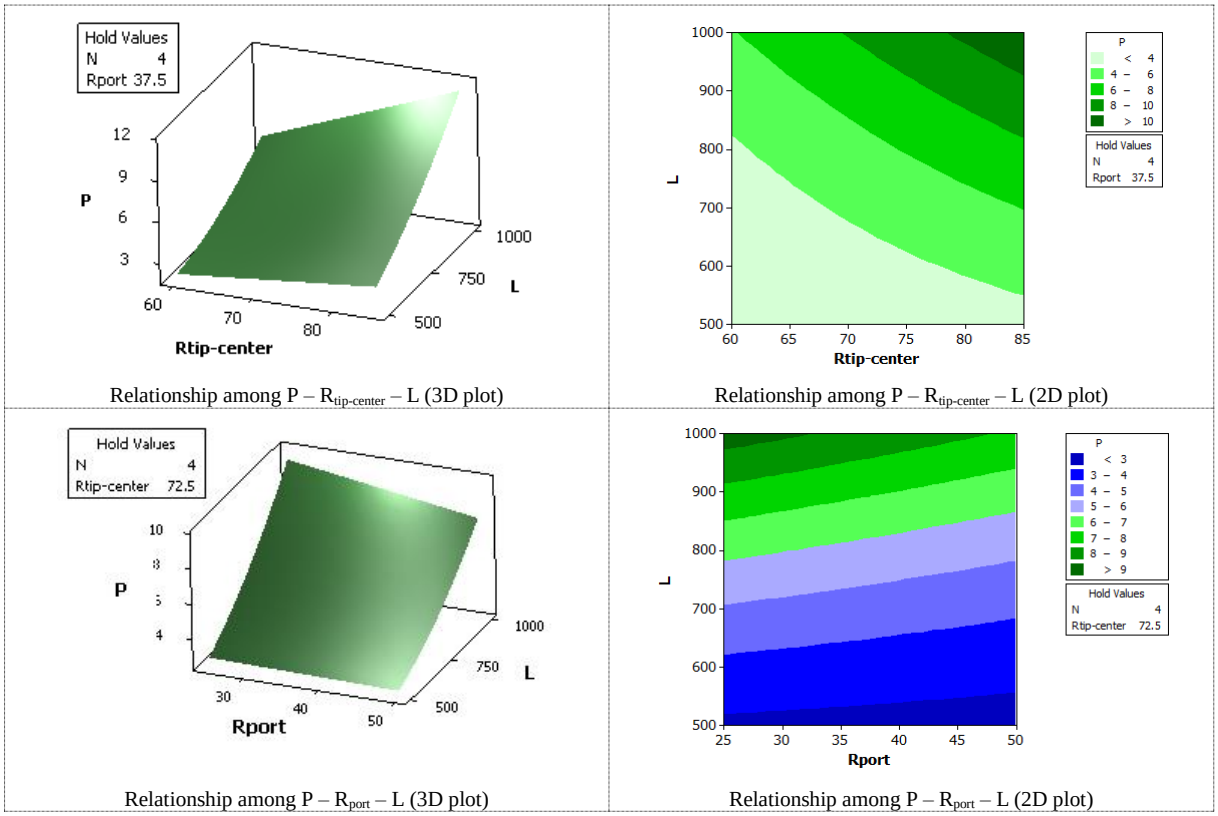

Relationship among P – $R_{tip\text{-}center}$ – L (3D plot)

Relationship among P – $R_{tip\text{-}center}$ – L (2D plot)

Relationship among P – R_{port} – L (3D plot)

Relationship among P – R_{port} – L (2D plot)

Fig. 19. Effects of parameters and interactions of them on chamber pressure value at the first steepest peak point (P).

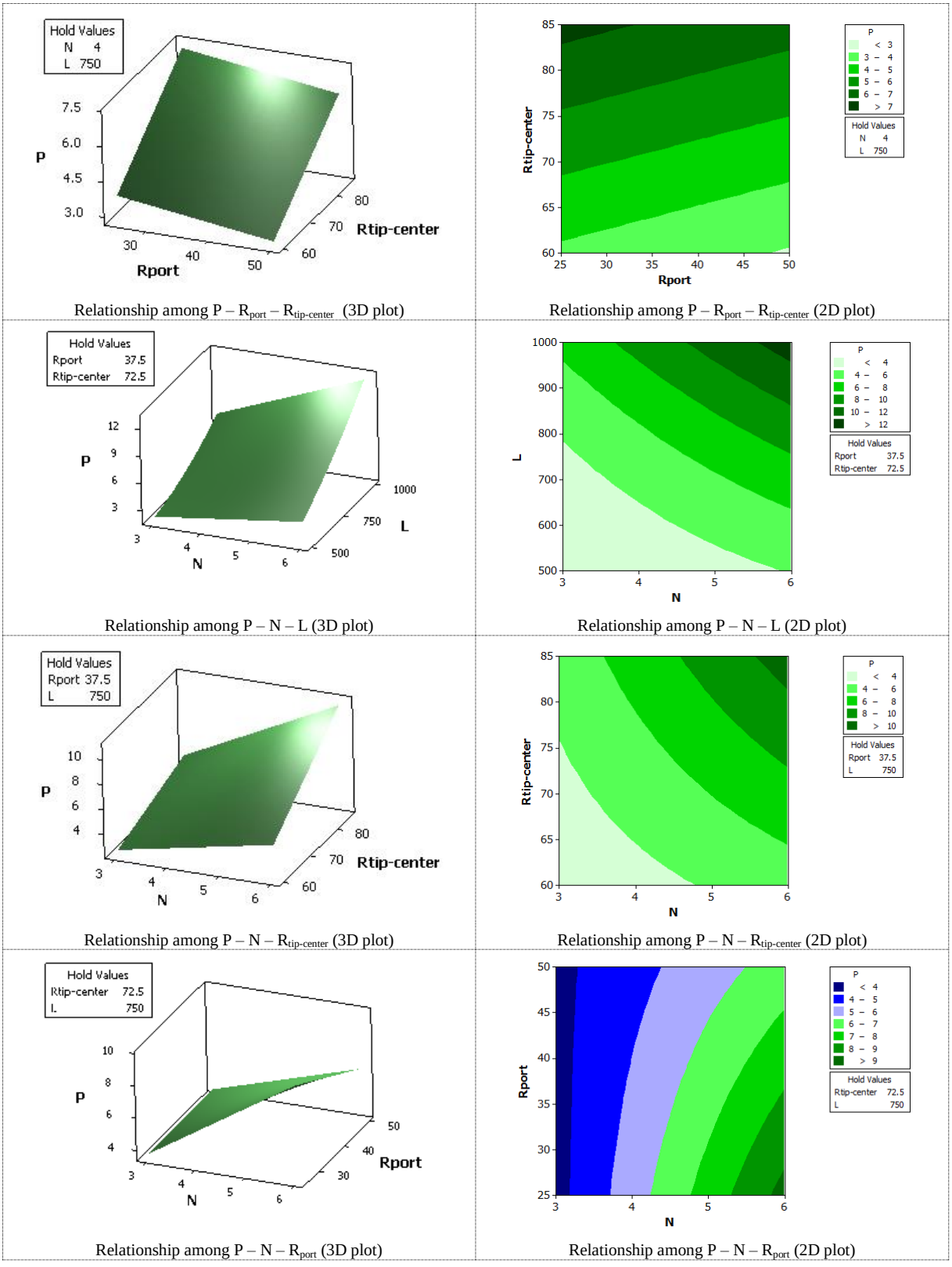

Fig. 19 (continued). Effects of parameters and interactions of them on chamber pressure value at the first steepest peak point (*P*).

Fig. 18 and Fig. 19 can be commented as follows:

- Length of the propellant (*L*) has the greatest effect on the variation of chamber pressure value at the first steepest peak point (*P*).
- Increment of length (*L*), number of slots (*N*) and slot length ($R_{tip\text{-}center}$) increases chamber pressure value at the first steepest peak point (*P*).

9.1.3. *Response surface of rise time (t_{rise})corresponding to P parameter*

Rise time (t_{rise}) corresponding to chamber pressure value at the first steepest peak point (P) is one another significant parameter that should be examined since this parameter has a critical importance on structural strength results of the viscoelastic propellant.

Fig. 20 represents the percentage effects of sectional parameters and interactions of them on rise time (t_{rise}) corresponding to P value.

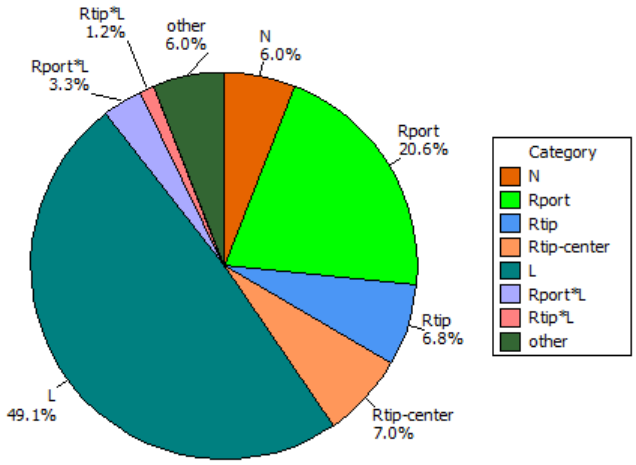

Fig. 20. Effects of sectional Parameters and interactions of them on rise time (t_{rise}) corresponding to P parameter.

Fig. 21 represents the variation of rise time (t_{rise}) corresponding to chamber pressure value at the first steepest peak point (P) with respect to sectional parameters.

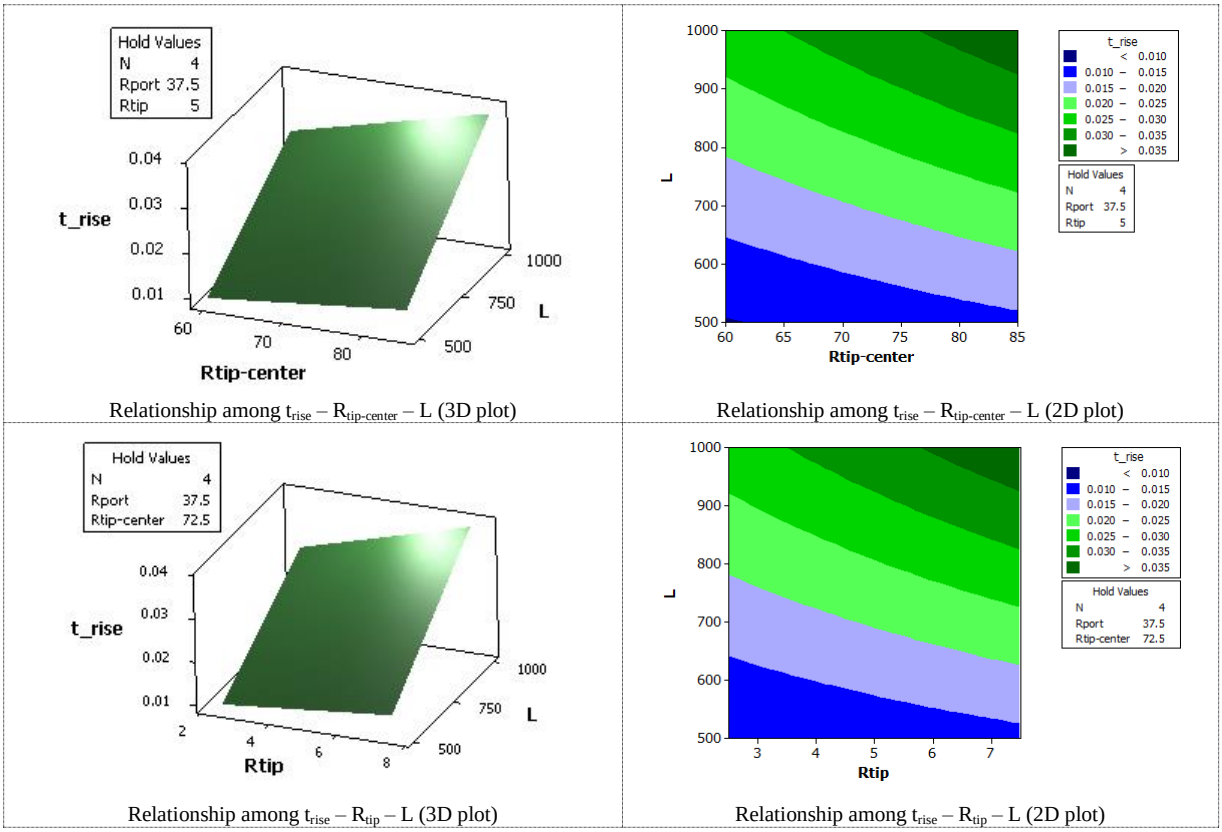

Fig. 21. Effects of sectional parameters and interactions of them on rise time (t_{rise}) corresponding to P parameter.

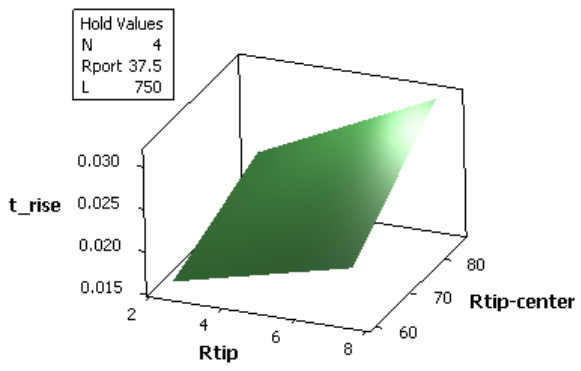

Relationship among t_{rise} – R_{tip} – $R_{tip\text{-}center}$ (3D plot)

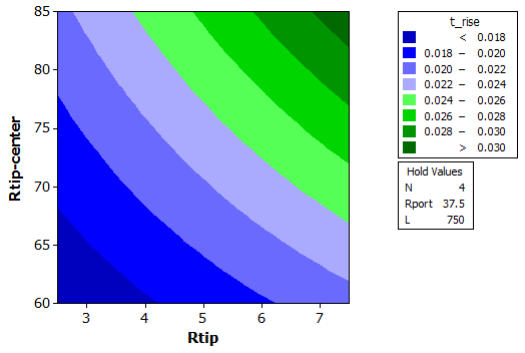

Relationship among t_{rise} – R_{tip} – $R_{tip\text{-}center}$ (2D plot)

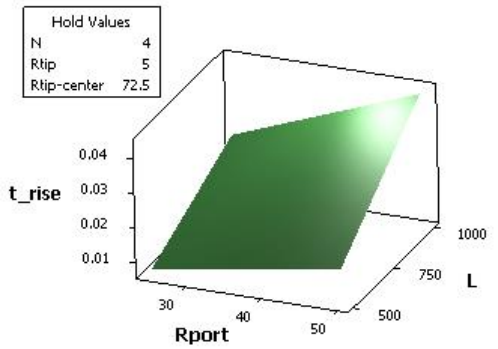

Relationship among t_{rise} – R_{port} – L (3D plot)

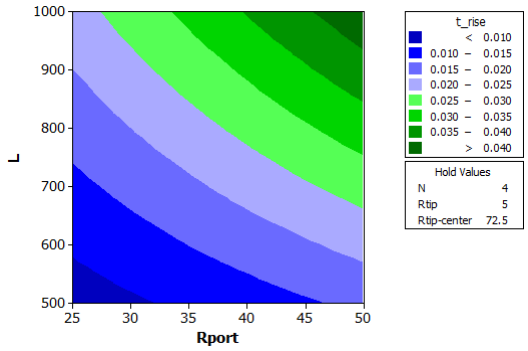

Relationship among t_{rise} – R_{port} – L(2D plot)

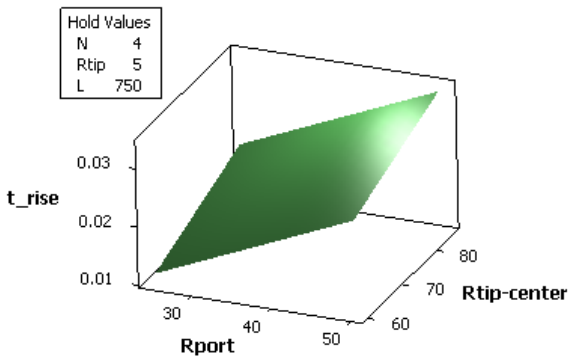

Relationship among t_{rise} – R_{port} – $R_{tip\text{-}center}$ (3D plot)

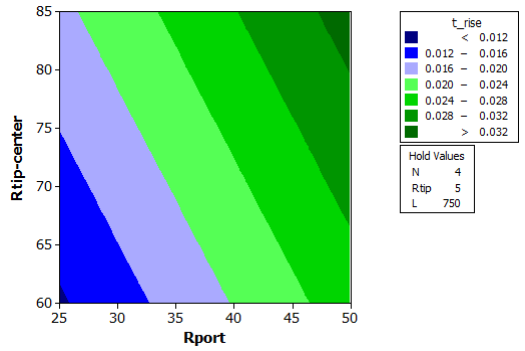

Relationship among t_{rise} – R_{port} – $R_{tip\text{-}center}$ (2D plot)

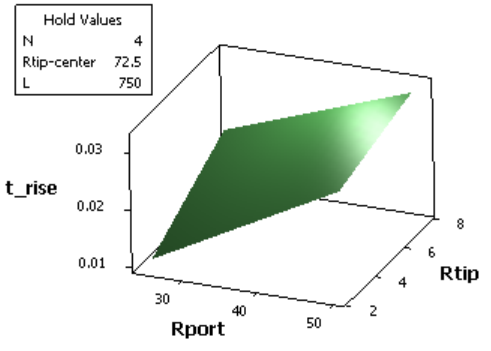

Relationship among t_{rise} – R_{port} – R_{tip} (3D plot)

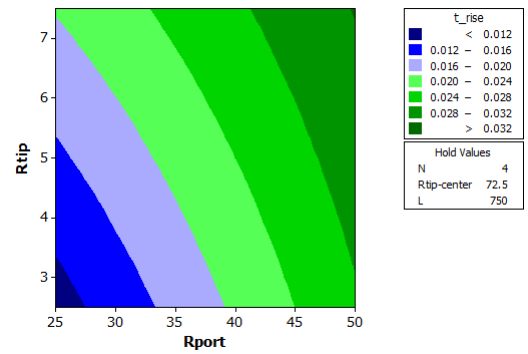

Relationship among t_{rise} – R_{port} – R_{tip} (2D plot)

Fig. 21 (continued). Effects of sectional parameters and interactions of them on rise time (t_{rise}) corresponding to *P* parameter.

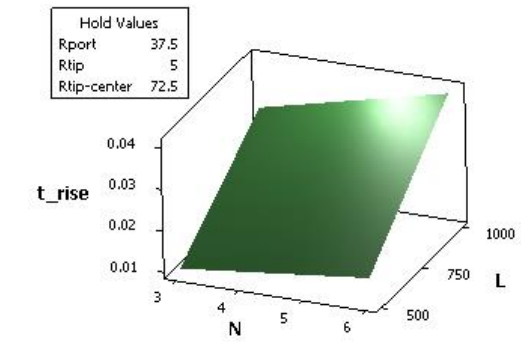

Relationship among t_{rise} – N – L (3D plot)

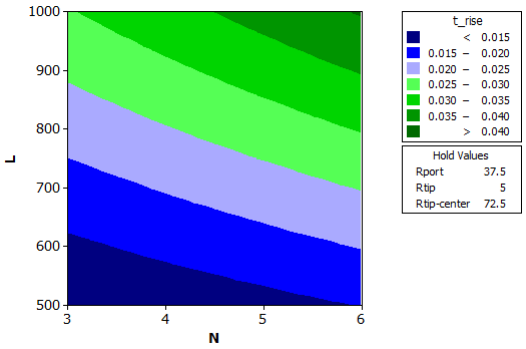

Relationship among t_{rise} – N – L (2D plot)

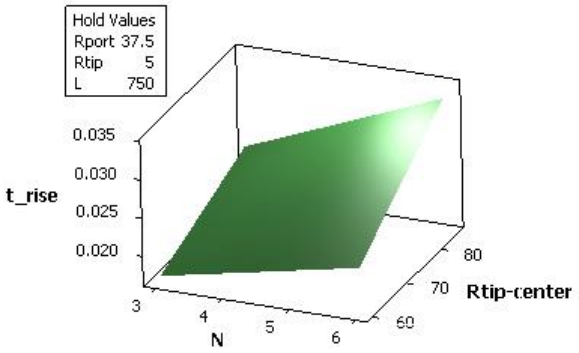

Relationship among t_{rise} – N – $R_{tip\text{-}center}$ (3D plot)

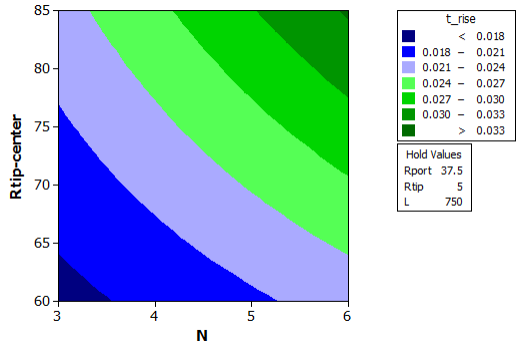

Relationship among t_{rise} – N – $R_{tip\text{-}center}$ (2D plot)

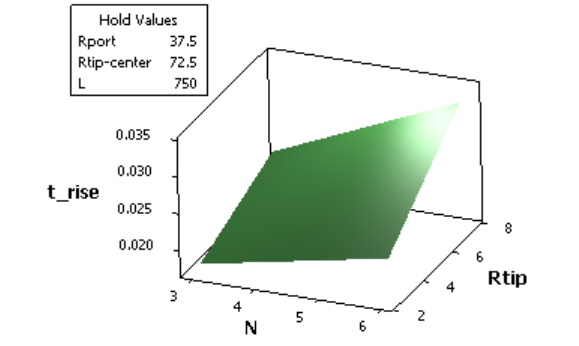

Relationship among t_{rise} – N – R_{tip} (3D plot)

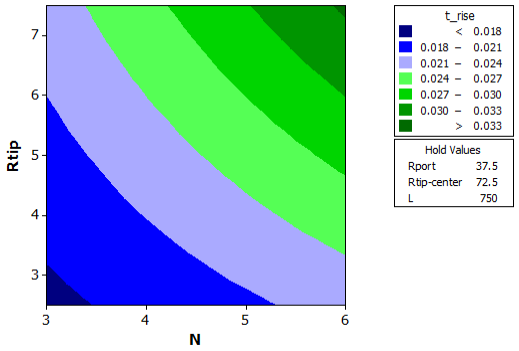

Relationship among t_{rise} – N – R_{tip} (2D plot)

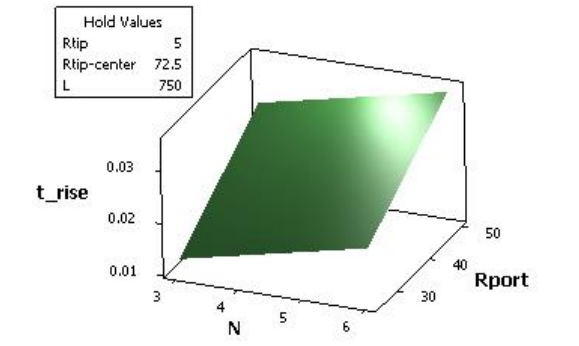

Relationship among t_{rise} – N – R_{port} (3D plot)

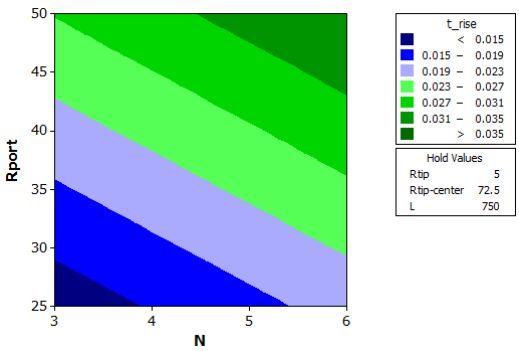

Relationship among t_{rise} – N – R_{port} (2D plot)

Fig. 21 (continued). Effects of sectional parameters and interactions of them on rise time (t_{rise}) corresponding to *P* parameter.

Fig. 20 and Fig. 21 can be commented as follows:

- Length of the propellant (*L*) has the greatest effect on the variation of rise time (t_{rise}) corresponding to chamber pressure value at the first steepest peak point (*P*).

- Port radius (R_{port}) also has a considerable amount of effect on t_{rise}.
- Increment of length (L), port radius (R_{port}), number of slots (N), slot length ($R_{tip\text{-}center}$), and tip radius (R_{tip}) increases rise time (t_{rise}) corresponding to chamber pressure value at the first steepest peak point (P).

Higher rise time (t_{rise}) implicitly increases the strength of the design.

9.1.4. *Response surface of propellant mass*

Fig. 22 represents the percentage effects of sectional parameters and interactions of them on propellant mass.

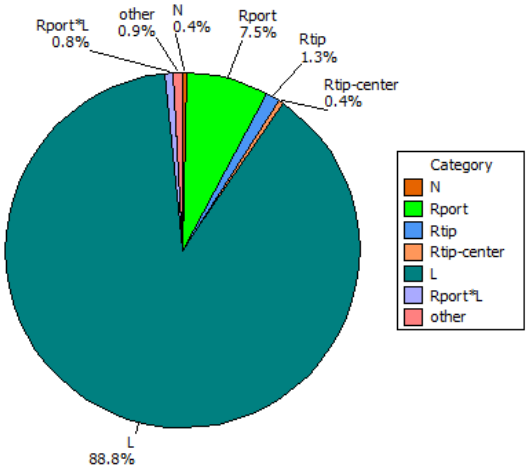

Fig. 22. Effects of sectional parameters and interactions of them on propellant mass.

Fig. 23 represents the variation of propellant mass with respect to sectional parameters.

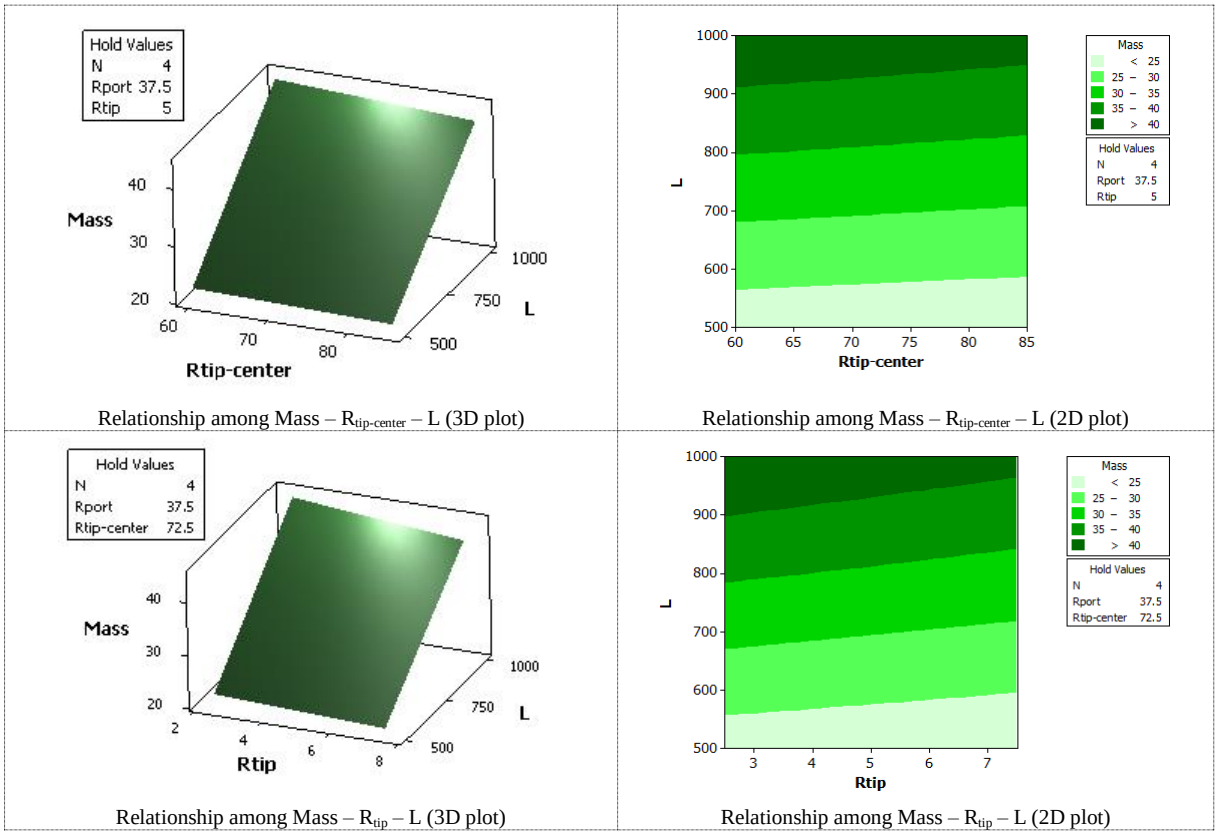

Relationship among Mass – $R_{tip\text{-}center}$ – L (3D plot)

Relationship among Mass – $R_{tip\text{-}center}$ – L (2D plot)

Relationship among Mass – R_{tip} – L (3D plot)

Relationship among Mass – R_{tip} – L (2D plot)

Fig. 23. Effects of sectional parameters and interactions of them on propellant mass.

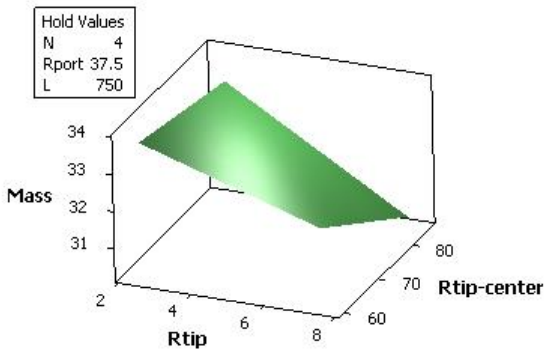

Relationship among Mass – R_{tip} – $R_{tip\text{-}center}$ (3D plot)

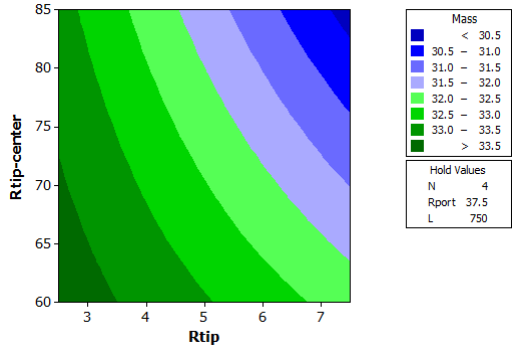

Relationship among Mass – R_{tip} – $R_{tip\text{-}center}$ (2D plot)

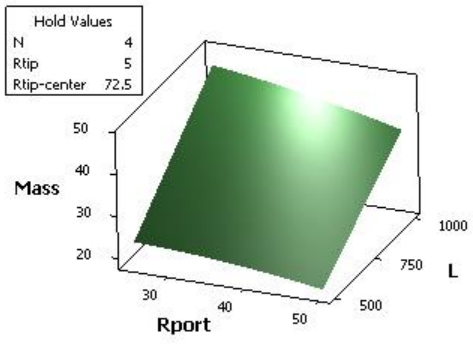

Relationship among Mass – R_{port} – L (3D plot)

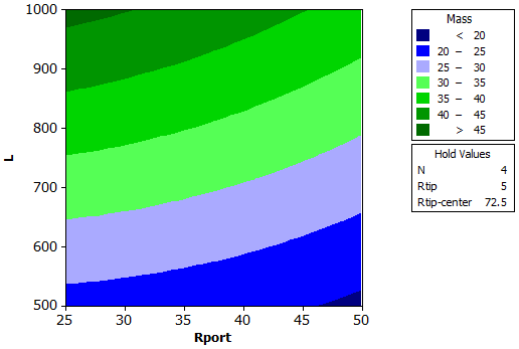

Relationship among Mass – R_{port} – L (2D plot)

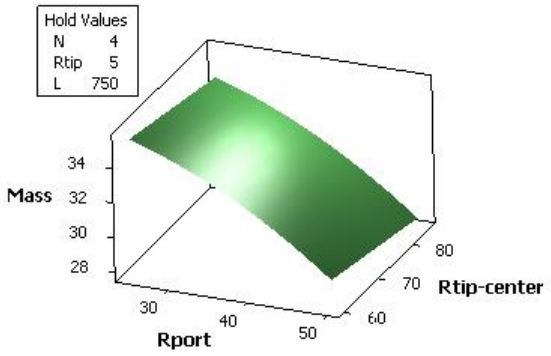

Relationship among Mass – R_{port} – $R_{tip\text{-}center}$ (3D plot)

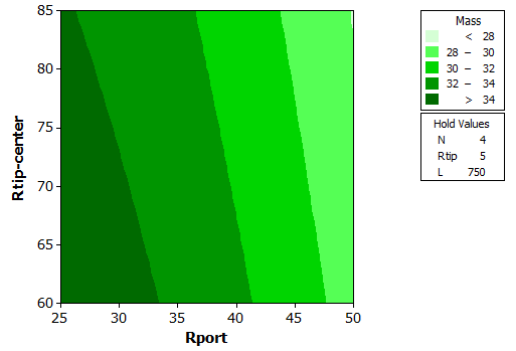

Relationship among Mass – R_{port} – $R_{tip\text{-}center}$ (2D plot)

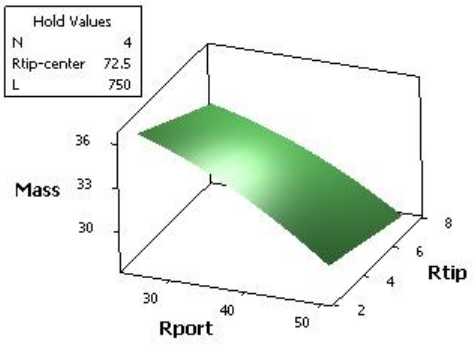

Relationship among Mass – R_{port} – R_{tip} (3D plot)

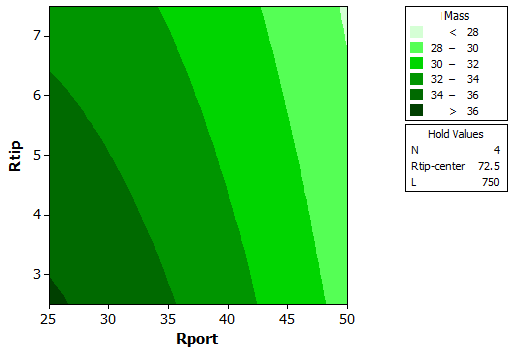

Relationship among Mass – R_{port} – R_{tip} (2D plot)

Fig. 23 (continued). Effects of sectional parameters and interactions of them on propellant mass.

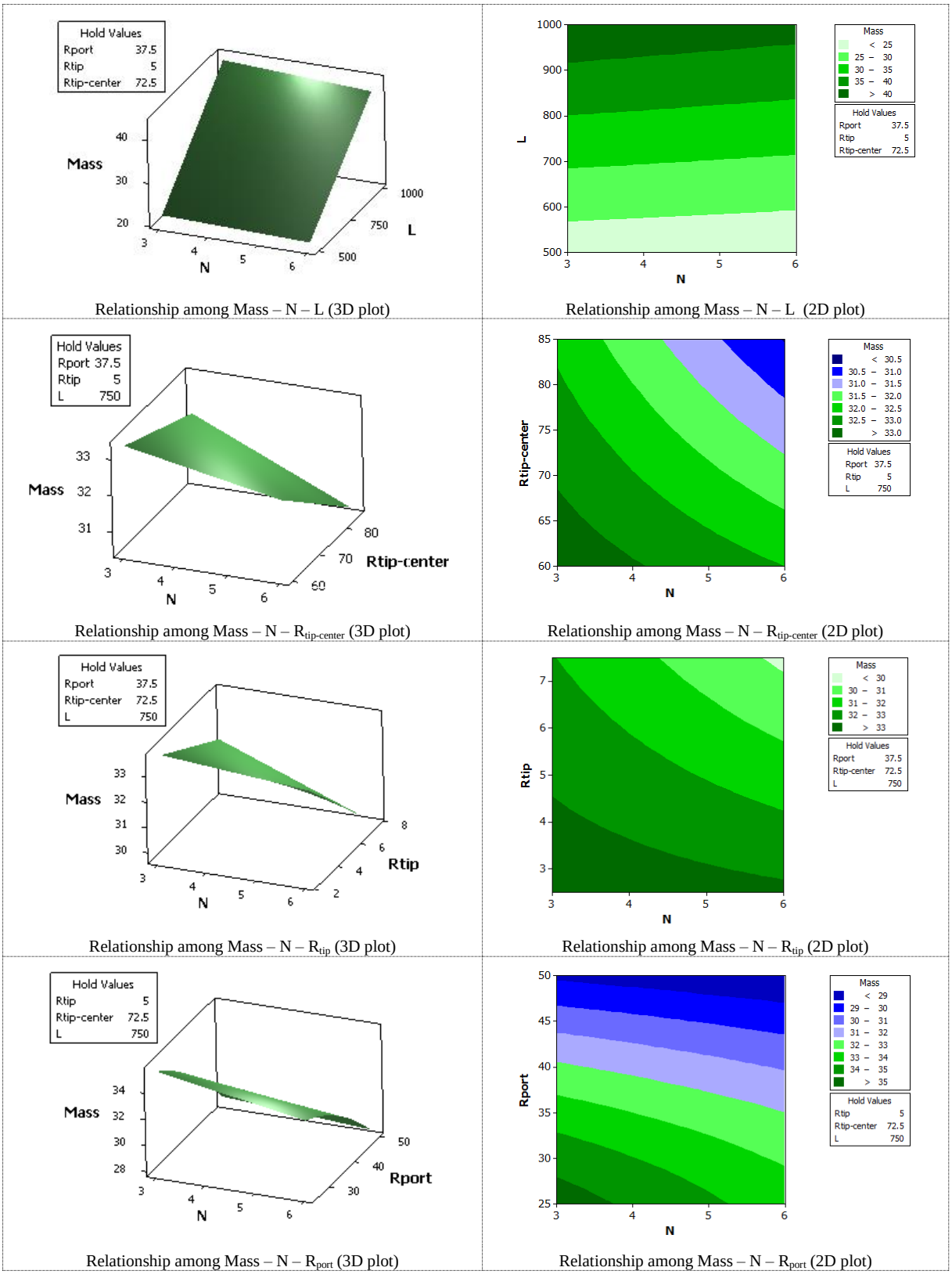

Relationship among Mass – N – L (3D plot)

Relationship among Mass – N – L (2D plot)

Relationship among Mass – N – $R_{tip\text{-}center}$ (3D plot)

Relationship among Mass – N – $R_{tip\text{-}center}$ (2D plot)

Relationship among Mass – N – R_{tip} (3D plot)

Relationship among Mass – N – R_{tip} (2D plot)

Relationship among Mass – N – R_{port} (3D plot)

Relationship among Mass – N – R_{port} (2D plot)

Fig. 23 (continued). Effects of sectional parameters and interactions of them on propellant mass.

Fig. 22 and Fig. 23 can be commented as follows:

- Length of the propellant (L) has the greatest effect on propellant mass.
- Port radius (R_{port}) also has a considerable amount of effect on propellant mass.
- Increment of length (L) and slot length ($R_{tip\text{-}center}$) increases propellant mass as expected.

- Increment of port radius (R_{port}), number of slots (N), and tip radius (R_{tip}) decreases propellant mass since they decrease volumetric loading of the rocket motor as expected.

9.2. *Response Surfaces Belonging to Finite Element Analysis Results*

In this sub-section, 2 different response surface analysis are performed using the finite element analysis results belonging to end of the ignition step to have an idea about how sectional parameters affect the structural strength of the propellant.

9.2.1. *Response surface of effective strain*

Maximum principal (ε_1), mid. principal (ε_2) and minimum principal (ε_3) strain values are determined as a result of finite element analysis within the content of this work. After that, effective strain (ε_{eff}) is calculated using these results as it is shown in Equation (23).

$$\varepsilon_{eff} = \frac{\sqrt{2}}{3}\sqrt{(\varepsilon_1-\varepsilon_2)^2+(\varepsilon_1-\varepsilon_3)^2+(\varepsilon_2-\varepsilon_3)^2} \tag{23}$$

Fig. 24 represents the percentage effects of sectional parameters and interactions of them on effective strain results belonging to end of the ignition step.

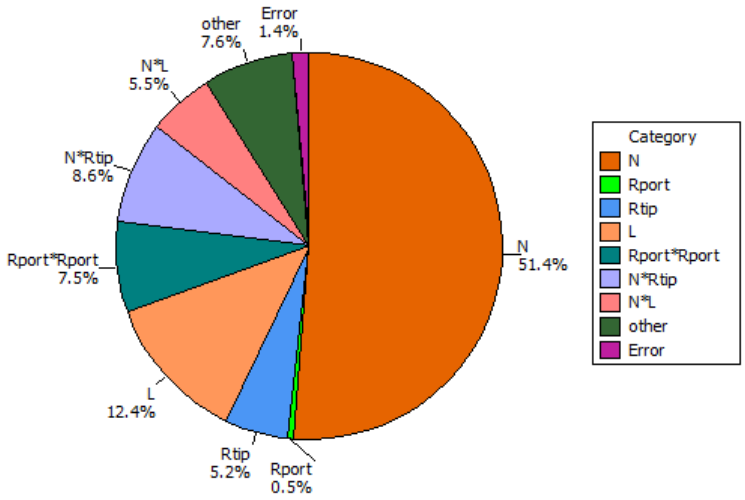

Fig. 24. Effects of sectional parameters and interactions of them on effective strain results belonging to end of the ignition step.

Fig. 25 represents the variation of effective strain results belonging to end of the ignition step with respect to sectional parameters.

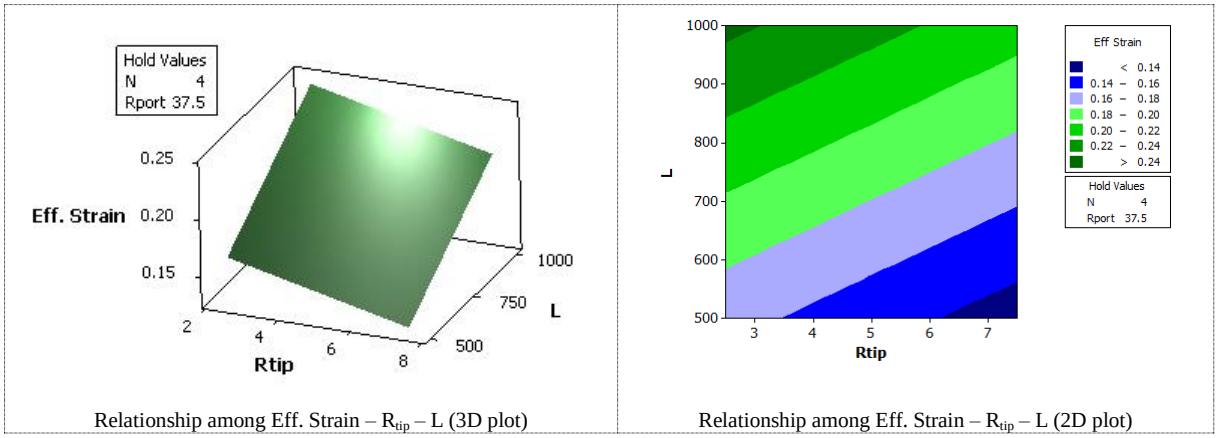

Relationship among Eff. Strain – R_{tip} – L (3D plot)

Relationship among Eff. Strain – R_{tip} – L (2D plot)

Fig. 25. Effects of sectional parameters and interactions of them on effective strain results belonging to end of the ignition step.

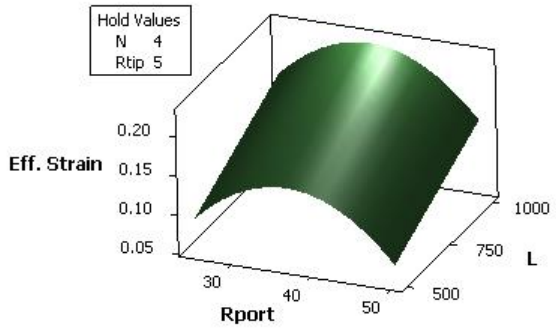

Relationship among Eff. Strain – R_{port} – L (3D plot)

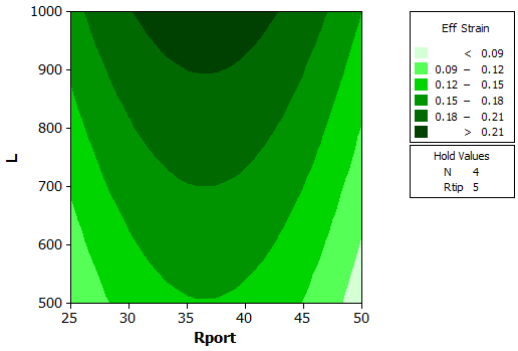

Relationship among Eff. Strain – R_{port} – L (2D plot)

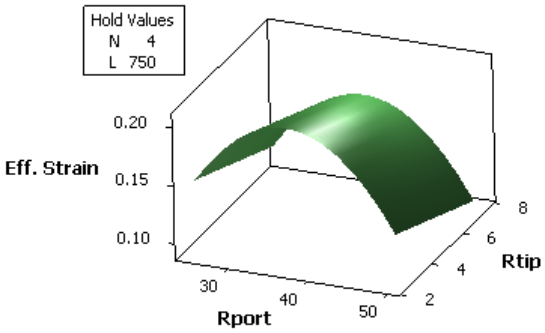

Relationship among Eff. Strain – R_{port} – R_{tip} (3D plot)

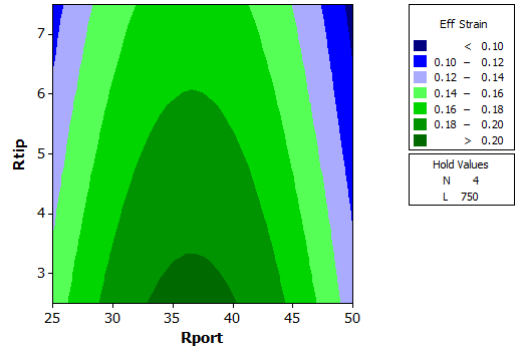

Relationship among Eff. Strain – R_{port} – R_{tip} (2D plot)

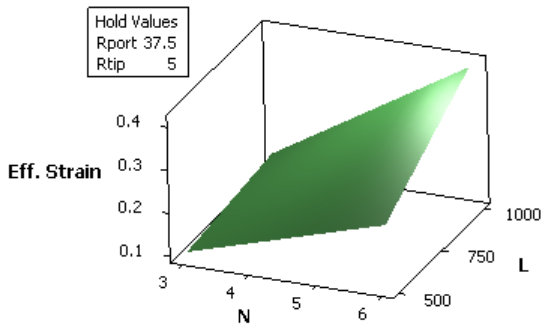

Relationship among Eff. Strain – N – L (3D plot)

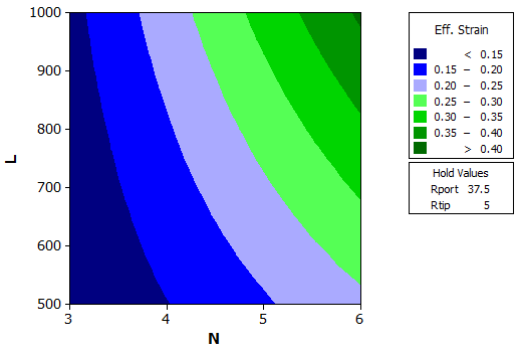

Relationship among Eff. Strain – N – L (2D plot)

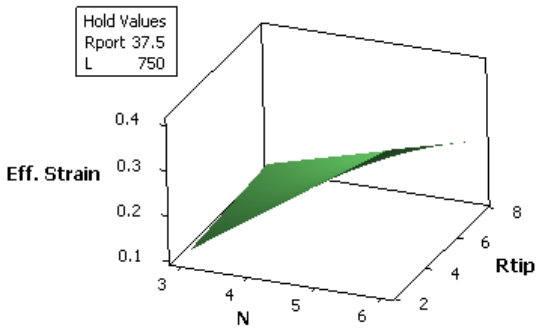

Relationship among Eff. Strain – N – R_{tip} (3D plot)

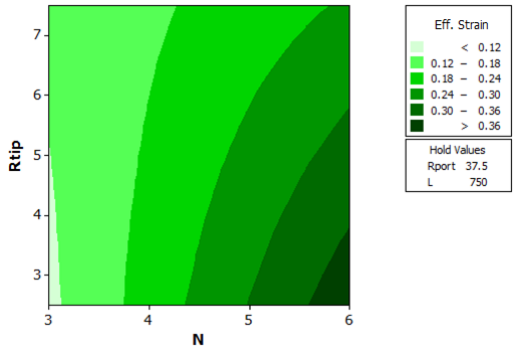

Relationship among Eff. Strain – N – R_{tip} (2D plot)

Fig. 25 (continued). Effects of sectional parameters and interactions of them on effective strain results belonging to end of the ignition step.

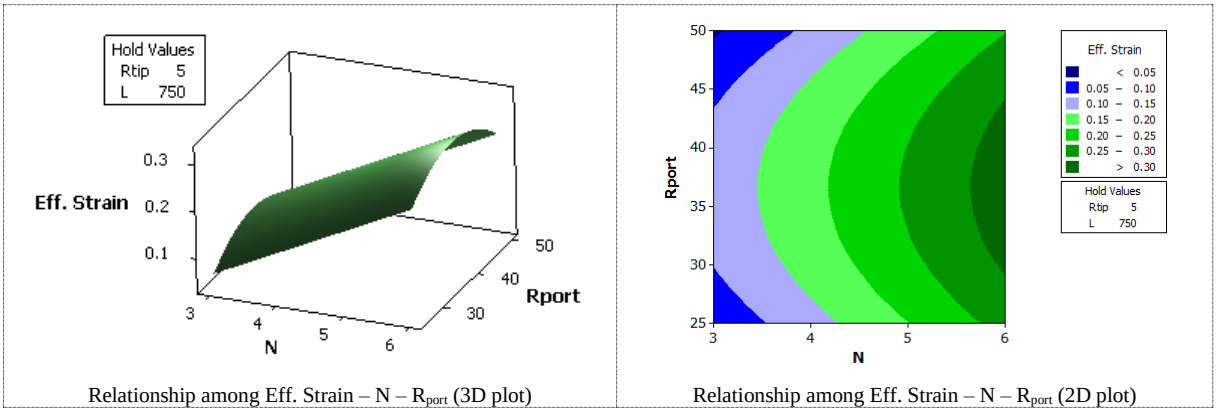

Relationship among Eff. Strain – N – R_{port} (3D plot)

Relationship among Eff. Strain – N – R_{port} (2D plot)

Fig. 25 (continued). Effects of sectional parameters and interactions of them on effective strain results belonging to end of the ignition step.

Fig. 24 and Fig. 25 can be commented as follows:

- Number of slots (*N*) has the greatest effect on the effective strain results.
- Length (*L*) also has a considerable amount of effect on the effective strain results since it changes burning area of the propellant sharply.
- Decrement of length (*L*) decreases the effective strain results since it decreases the value of chamber pressure at the first steepest peak point (*P*).
- Decrement of the number of slots (N) leads to the decrement of the effective strain since this decrement leads to both decreases the burnings area of the propellant and increases the stiffness of the propellant design.
- Increment of tip radius (R_{tip}) decreases the effective strain since it increases the radius at the critical point.

9.2.2. *Response surface of Von Misses stress*

Fig. 26 represents the percentage effects of sectional parameters and interactions of them on Von Misses stress results belonging to end of the ignition step.

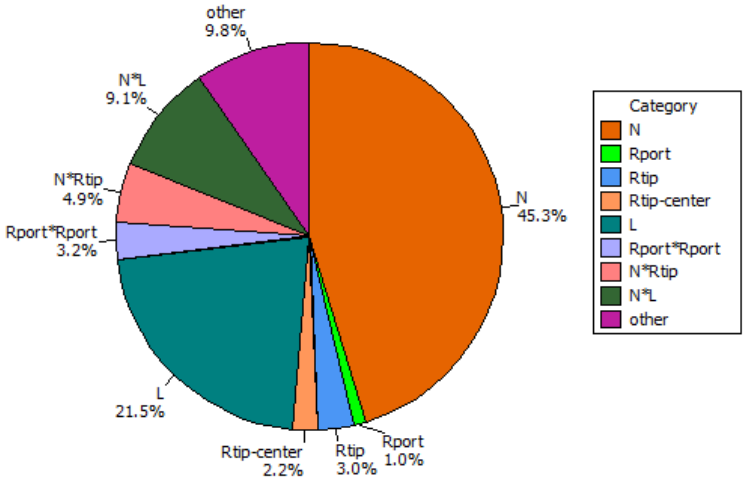

Fig. 26. Effects of sectional parameters and interactions of them on Von Misses stress results belonging to end of the ignition step.

Fig. 27 represents the variation of Von Misses stress results belonging to end of the ignition step with respect to sectional parameters.

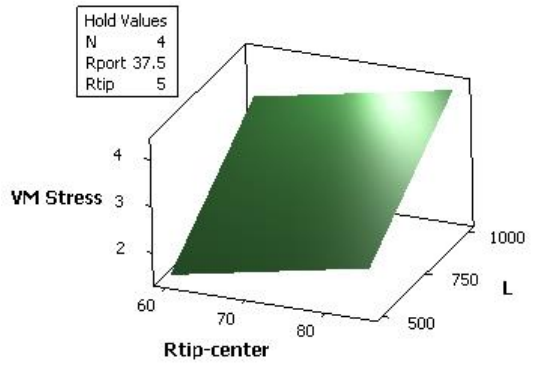

Relationship among VM. Stress – $R_{tip\text{-}center}$ – L (3D plot)

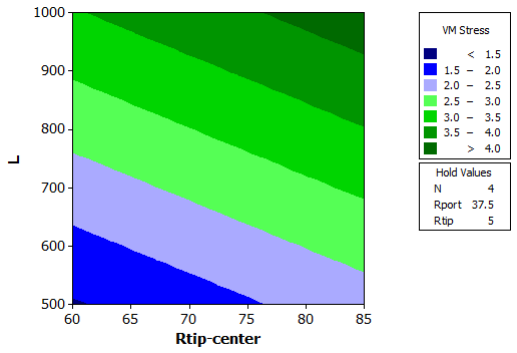

Relationship among VM. Stress – $R_{tip\text{-}center}$ – L (2D plot)

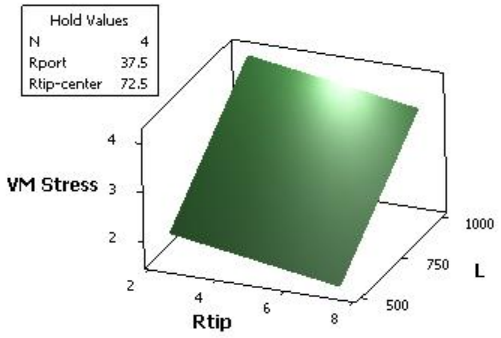

Relationship among VM. Stress – R_{tip} – L (3D plot)

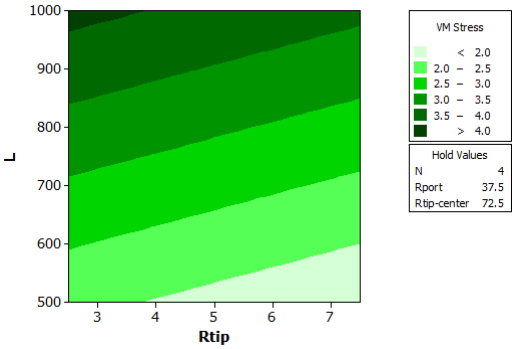

Relationship among VM. Stress – R_{tip} – L (2D plot)

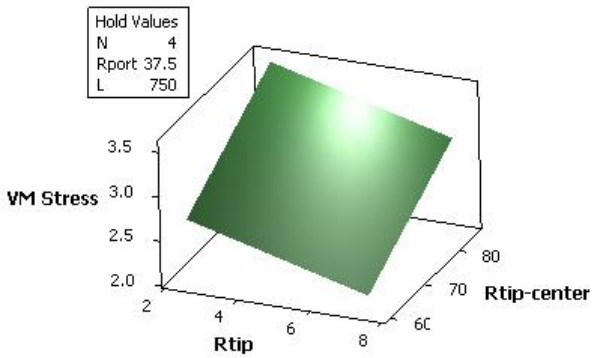

Relationship among VM. Stress – R_{tip} – $R_{tip\text{-}center}$ (3D plot)

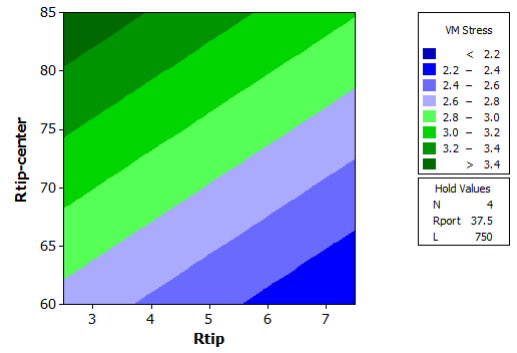

Relationship among VM. Stress – R_{tip} – $R_{tip\text{-}center}$ (2D plot)

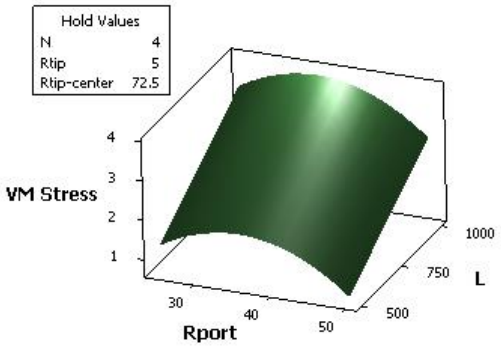

Relationship among VM. Stress – R_{port} – L (3D plot)

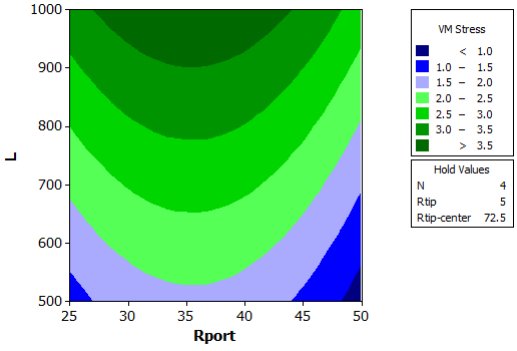

Relationship among VM. Stress – R_{port} – L (2D plot)

Fig. 27. Effects of sectional parameters and interactions of them on Von Misses stress results belonging to end of the ignition step.

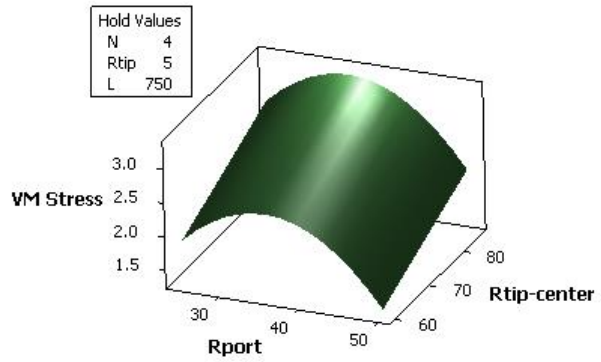

Relationship among VM. Stress – R_{port} – $R_{tip\text{-}center}$ (3D plot)

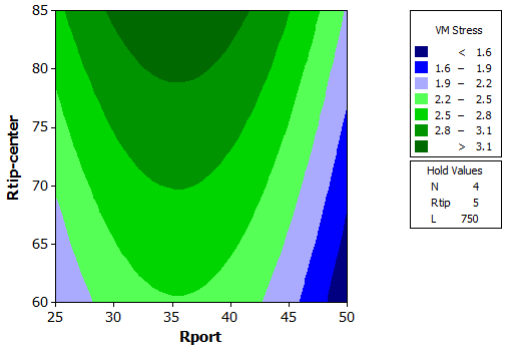

Relationship among VM. Stress – R_{port} – $R_{tip\text{-}center}$ (2D plot)

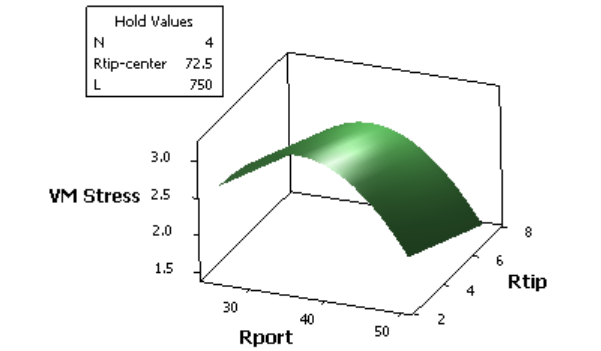

Relationship among VM. Stress – R_{port} – R_{tip} (3D plot)

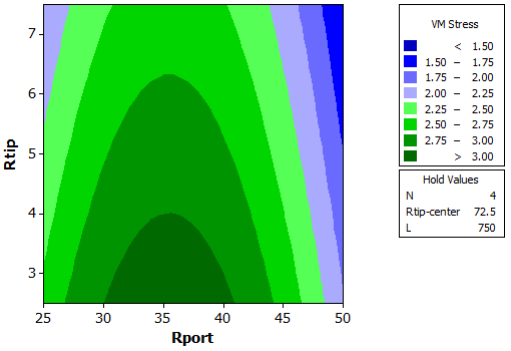

Relationship among VM. Stress – R_{port} – R_{tip} (2D plot)

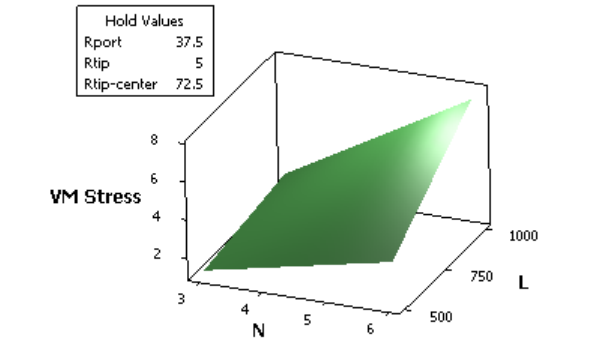

Relationship among VM. Stress – N – L (3D plot)

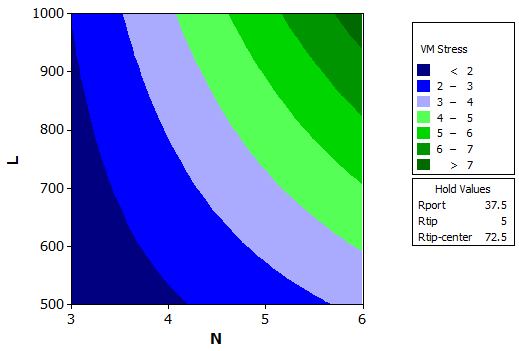

Relationship among VM. Stress – N – L (2D plot)

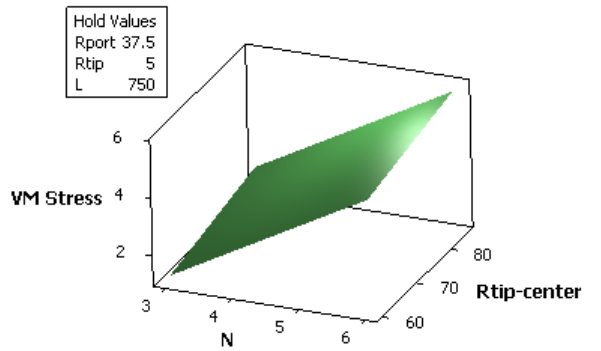

Relationship among VM. Stress – N – $R_{tip\text{-}center}$ (3D plot)

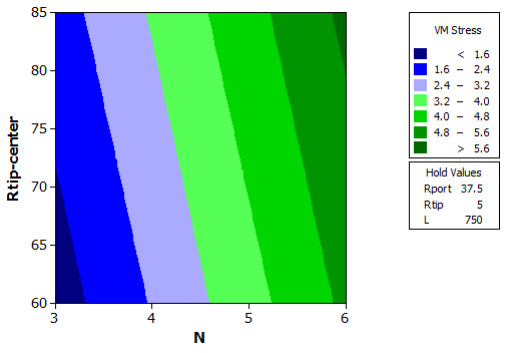

Relationship among VM. Stress – N – $R_{tip\text{-}center}$ (2D plot)

Fig. 27 (continued). Effects of sectional parameters and interactions of them on Von Misses stress results belonging to end of the ignition step.

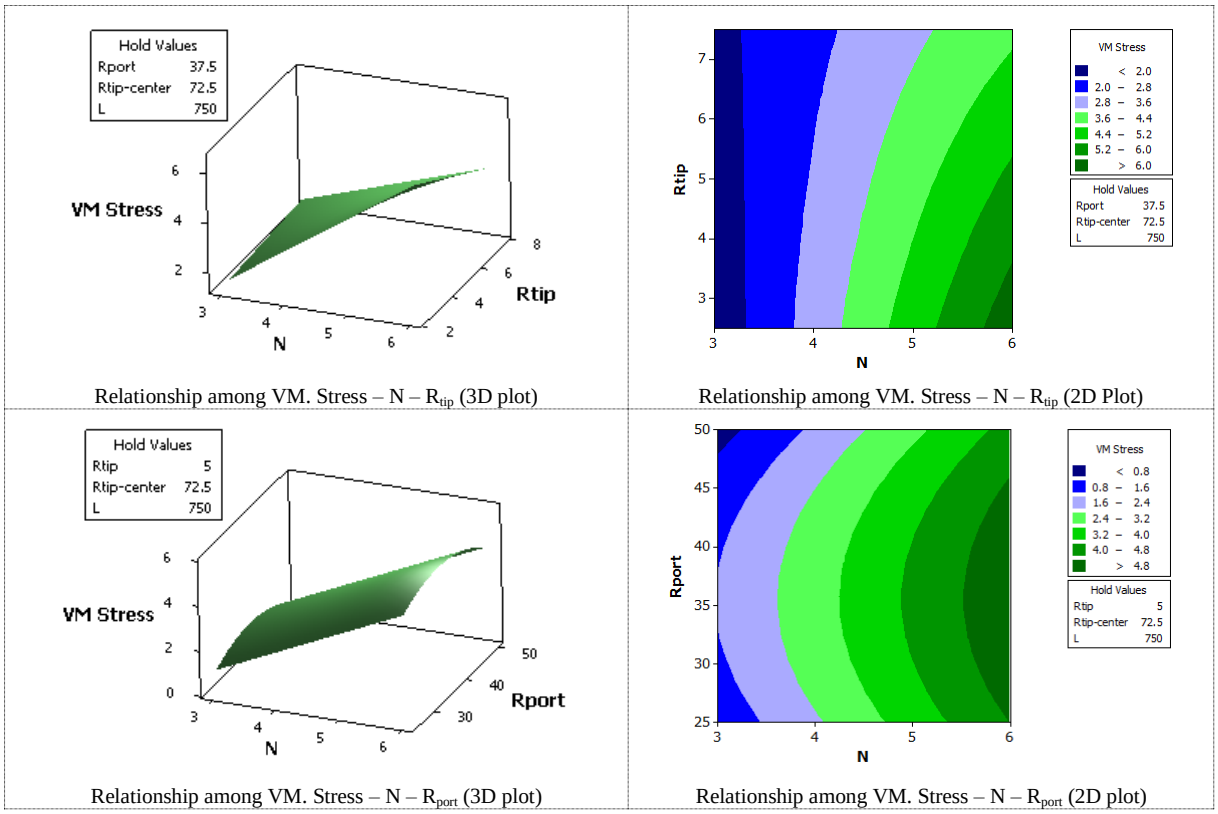

Relationship among VM. Stress – N – R_{tip} (3D plot)

Relationship among VM. Stress – N – R_{tip} (2D Plot)

Relationship among VM. Stress – N – R_{port} (3D plot)

Relationship among VM. Stress – N – R_{port} (2D plot)

Fig. 27 (continued). Effects of sectional parameters and interactions of them on Von Misses stress results belonging to end of the ignition step.

Fig. 26 and Fig. 27 can be commented as follows:

- Number of slots (*N*) has the greatest effect on the Von Misses stress results.
- Length (*L*) also has a considerable amount of effect on the Von Misses stress results since it changes burning area of the propellant sharply.
- Decrement of length (*L*) decreases the Von Misses stress results since it decreases the value of chamber pressure at the first steepest peak point (*P*).
- Decrement of the number of slots (*N*) leads to decrement of the Von Misses stress since this leads to reduce the burnings area of the propellant and increase the stiffness of the propellant design.
- Increment of tip radius (R_{tip}) decreases the Von Misses stress results since it increases the radius at the critical point.
- Decrement of slot length ($R_{tip\text{-}center}$) slightly decreases the Von Misses stress results.

10. Concluding Remarks

Within the content of this work, effects of sectional geometric parameters of a slotted HTPB based solid propellant on its internal ballistic performance and structural strength is examined using zero dimensional ballistic solver and finite element analysis with the assistance of response surface method. First, coupled solution systematic of internal ballistic performance analysis and finite element analysis are explained. After that, performing numerous analysis, graphical results that may be useful for solid rocket motor designers are determined. Percentage effects of sectional geometric parameters on response variables are examined. Thus, it is revealed that which actions has to be taken in order to increase the performance of a solid rocket motor and to decrease the strain and stress values on the propellant.

Response surface method is one of the efficient ways that can be used to evaluate the relation between explanatory variables with response variables. Thus, it is possible to gaining the time spent on response surface construction period in the subsequent phases of a design project by prohibiting the iterations governing from the erroneous design parameter selection.

References

Acik, S. (2010). Internal Ballistic Design Optimization of a Solid Rocket Motor. M.Sc. Dissertation, Mechanical Engineering Dept., Middle East Technical Univ., Ankara.

Advisory Group for Aerospace Research and Development (AGARD). (1997). *Structural Assessment of Solid Propellant Grains*. AGARD-AR-350.

ASTM International, (2001). Standard Test Method for Determining Specific Heat Capacity by Diffrential Scanning Calorimetry. ASTM Standard E 1269-01.

ASTM International. (2003). Standard Test Method for Linear Thermal Expansion of Solid Materials by Thermomechanical Analysis. ASTM Standard E 831-03.

Gandia, A. J. (2012). *A Phased Trade Study for the Design of a Solid Rocket Motor*. M.Sc. Dissertation. Mechanical Engineering Dept. Rensselaer Polytechnic Institute. Hartford. Connecticut.

Incropera, F. P., and DeWitt, D. P. (2007). *Fundamentals of Heat and Mass Transfer*. Translation from 4th Edition. Literatür Yayınları. İstanbul.

Lakes, R. S. (1999). *Viscoelastic Solids*. CRC-Press.

NATO Standardization Agency. (2000). STANAG 4506 PPS (Ed. 1) Explosives, Physical / Mechanical Properties Uniaxial Tensile Test.

NATO Standardization Agency. (2002). STANAG 4507 PCS (Ed. 1) Explosives, Physical / Mechanical Properties Stress Relaxation Test in Tension.

Ozgen, G. O. (2010). ME 708 Techniques for Vibration Control and Isolation Lecture Notes. Middle East Technical Univ. Ankara.

Sutton, G. P. and Biblarz, O. (2001). *Rocket Propulsion Elements*. 7th edn. John Wiley & Sons. New York.

Ward, T. (2010). *Aerospace Propulsion Systems*, 1st edn. John Wilet & Sons (Asia) Pte. Ltd. Singapore.